

## Upscale Evolution of MCSs: Doppler Radar Analysis and Analytical Investigation

RAY L. MCANELLY, JASON E. NACHAMKIN, WILLIAM R. COTTON, AND MELVILLE E. NICHOLLS

*Department of Atmospheric Science, Colorado State University, Fort Collins, Colorado*

(Manuscript received 5 March 1996, in final form 24 September 1996)

### ABSTRACT

The development of two small mesoscale convective systems (MCSs) in northeastern Colorado is investigated via dual-Doppler radar analysis. The first system developed from several initially isolated cumulonimbi, which gradually coalesced into a minimal MCS with relatively little stratiform precipitation. The second system developed more rapidly along an axis of convection and generated a more extensive and persistent stratiform echo and MCS cloud shield. In both systems, the volumetric precipitation rate exhibited an early meso- $\beta$ -scale convective cycle (a maximum and subsequent minimum), followed by reintensification into a modest mature stage. This sequence is similar to that noted previously in the developing stage of larger MCSs by McAnelly and Cotton. They speculated that the early meso- $\beta$  convective cycle is a characteristic feature of development in many MCSs that is dynamically linked to a rather abrupt transition toward mature stage structure. This study presents kinematic evidence in support of this hypothesis for these cases, as derived from dual-Doppler radar analyses over several-hour periods. Mature stage MCS characteristics such as deepened low- to midlevel convergence and mesoscale descent developed fairly rapidly, about 1 h after the early meso- $\beta$  convective maximum.

The dynamic linkage between the meso- $\beta$  convective cycle and evolution toward mature structure is examined with a simple analytical model of the linearized atmospheric response to prescribed heating. Heating functions that approximate the temporal and spatial characteristics of the meso- $\beta$  convective cycle are prescribed. The solutions show that the cycle forces a response within and near the thermally forced region that is consistent with the observed kinematic evolution in the MCSs. The initial response to an intensifying convective ensemble is a self-suppressing mechanism that partially explains the weakening after a meso- $\beta$  convective maximum. A lagged response then favors reintensification and areal growth of the weakened ensemble. A conceptual model of MCS development is proposed whereby the early meso- $\beta$  convective cycle and the response to it are hypothesized to act as a generalized forcing–feedback mechanism that helps explain the upscale growth of a convective ensemble into an organized MCS.

### 1. Introduction

In a study of the radar-inferred precipitation evolution of mesoscale convective complexes (MCCs; Maddox 1980), McAnelly and Cotton (1992; hereafter MC92) identified a characteristic meso- $\beta$ -scale burst or cycle of convective precipitation that is superimposed early on the meso- $\alpha$ -scale growth–decay life cycle in many systems (Fig. 1). They hypothesized that the cycle could be dynamically linked to a relatively rapid upscale evolution of many MCCs and mesoscale convective systems (MCSs) in general. Prior to this evolution, the early system is characterized by an ensemble of multiple convective cells and/or multicell clusters, each dominated by relatively independent, convective-scale circulations. The term “upscale evolution” is defined here as the development of organized mesoscale circulations and a

unifying stratiform echo on scales comparable to the entire convective ensemble and its common cirrus canopy. MC92 based their hypothesis on the fairly abrupt development of mature stage features following such a meso- $\beta$  convective cycle, as reported in observed cases and evident in simulated cases of MCSs that they cited in the literature. Mature stage features indicating an MCS having evolved upscale include deepened low-level convergence into midlevels, organized mesoscale outflow aloft, descending rear inflow, and a surface mesohigh and wake low. MC92 suggested that gravity wave dynamics played a prominent role in this evolution.

The idea that MCSs develop as a self-organizing system through forced gravity wave mechanisms has been explored in detail by Raymond (1983, 1984, 1986, 1987). His linearized models with parameterized convective effects have had some success in simulating propagation speeds and other observed aspects of MCSs. Some of his solutions indicate a sequence of convective development that evinces the  $\beta$ -scale convective cycle: growth of an initial advective instability mode, its weakening, and subsequent growth of a prop-

---

*Corresponding author address:* Ray L. McAnelly, Dept. of Atmospheric Science, Colorado State University, Fort Collins, CO 80523-1371.

E-mail: raymc@woxof.atmos.coloState.edu

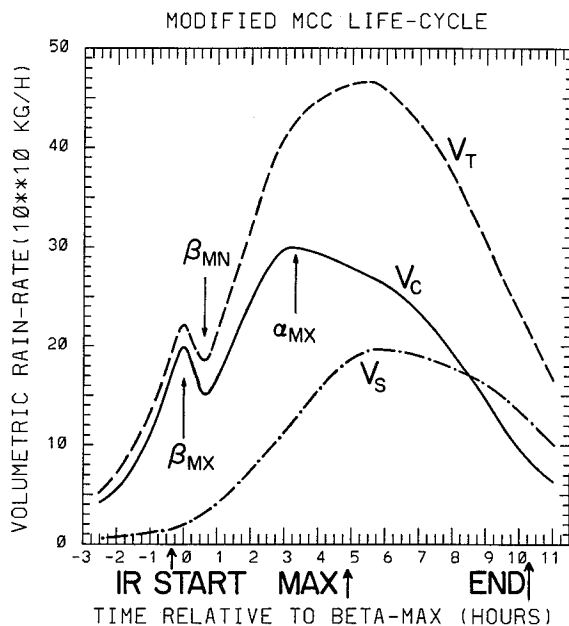


FIG. 1. Generalized MCC precipitation lifecycle, in terms of volumetric rain rate due to convective, stratiform, and total echo ( $V_C$ ,  $V_S$ , and  $V_T$ , respectively). An early meso- $\beta$ -scale convective cycle (labeled  $\beta_{MX}$  and  $\beta_{MN}$ ) is superimposed on the growth stage of the meso- $\alpha$ -scale lifecycle. Lifecycle benchmarks based on infrared satellite imagery are also indicated. From McAnelly and Cotton (1992).

agating instability mode (e.g., Raymond 1984, his Figs. 4 and 6; Raymond 1987, his Figs. 8 and 13). Raymond (1986) demonstrated that low-level evaporational cooling forced a destabilization (adiabatic lifting) in the lower atmosphere in the near environment, so that air feeding the convection was conditioned for further convection. Mapes (1993) described how this low-level ascent propagates into the environment and favors additional convection over a large area. Nonhydrostatic cloud modeling studies also indicate that gravity wave dynamics can significantly affect simulated MCSs. Tripoli and Cotton (1989a,b) found that meso- $\beta$ -scale gravity waves strongly modulated the intensity of a simulated long-lived orogenic MCS. Schmidt and Cotton (1990) showed that deep and lower-tropospheric gravity waves played a prominent role in a simulated squall line's development and structure in a sheared environment.

The first purpose of this study is to present kinematic evidence of rapid upscale evolution subsequent to an early meso- $\beta$ -scale convective cycle in two small MCSs that were observed in northeastern Colorado. The evidence primarily consists of the rapid appearance of deep midlevel convergence and concurrent development of mature stage vertical motion characteristics, temporally resolved from frequent dual-Doppler radar analyses over several-hour periods. While this development cannot definitely be linked to the preceding convective burst, the similar sequence of kinematic evolution in these two cases with markedly different reflectivity structure and evolution further supports the generalized upscale evo-

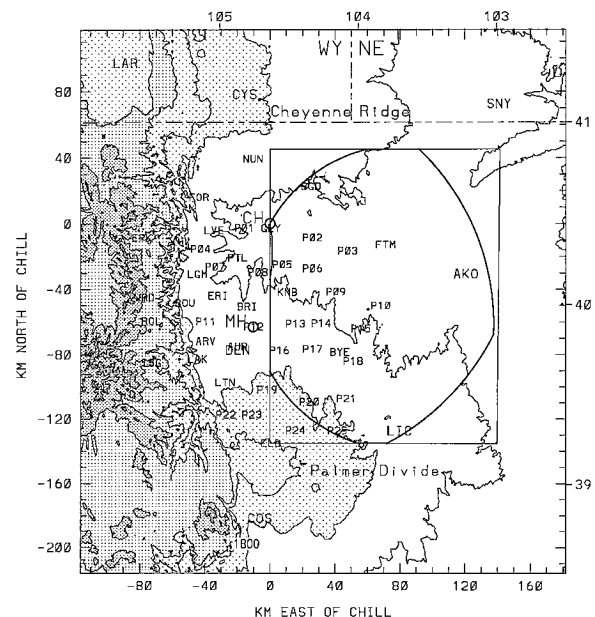


FIG. 2. Map of observational area in northeastern Colorado and adjacent portions of Wyoming (WY) and Nebraska (NE). CSU-CHILL and Mile High radars are at circles labeled CH and MH. The eastern dual-Doppler lobe and 140 km  $\times$  180 km analysis domain are shown. Surface observations include standard hourly data at large three-letter sites and 5-min mesonet data at smaller three-character sites. Topography includes contours (m) of 1200 (in northeast), 1500, 1800, 2100, 2400, 3000, and 3600, and progressively darker shades for elevations above 1800, 2400, 3000, and 3600 m.

lution scenario proposed by MC92. The dual-Doppler data and techniques used for this analysis are described in section 2. Sections 3 and 4 present analyses of the first and second cases, respectively.

The second purpose is to further explore the hypothesized dynamic linkage between the meso- $\beta$  convective cycle and the upscale evolution toward mature MCS structure. In section 5, the analytical linearized solutions of the two-dimensional (2D) atmospheric response to prescribed heating, developed by Nicholls et al. (1991) and discussed further by Mapes (1993), are used to illustrate this dynamic linkage. It is shown that the linearized response to time-dependent heating that approximates the meso- $\beta$  convective cycle is similar to the kinematic evolution in the two observed MCSs. In section 6, a conceptual model of MCS development is presented: the linearized response to an intensifying convective ensemble is viewed as a forcing–feedback mechanism that helps explain its characteristic upscale evolution into a mature MCS. This model is compared and contrasted with forced gravity wave models and other conceptual models of developing MCSs.

## 2. Observational data and analysis methodology

A small radar field program (Fig. 2) was conducted during the late-July and early-August periods of 1992–

94, supported by the CSU-CHILL radar facility (Rutledge et al. 1993) near Greeley, Colorado. The objective was to collect dual-Doppler radar data on the growth stages of MCSs. Presented here are analyses for a case from 1992 and another from 1993. The other radar for the 1992–93 seasons was Mile High Radar (MHR; Pratte et al. 1991), a semi-operational NEXRAD prototype near Denver, operated by the National Center for Atmospheric Research (NCAR). During operational periods, CSU-CHILL collected full 360° volume scans every 6 min, synchronized with similar volume scans by MHR. Although MHR was on a rather long, 64-km north–south baseline with CSU-CHILL, successful dual-Doppler analyses using data from these radars has been performed on many convective storm systems (e.g., Kennedy and Rutledge 1995).

Both CSU-CHILL and MHR are S-band radars with approximately 1° beamwidths. Volume scans for CSU-CHILL consisted of 16 constant-elevation scans from approximately 0.5° to 26.5°, while MHR had 11 scans from 0.5° to 22°. Both radars collected data to approximately 150 km at 225 or 300 m gate spacing. The long baseline and 150-km range provided dual-Doppler coverage over large analysis lobes (defined liberally by a 20° beam-crossing angle), so that convection developing into MCSs remained in coverage over extended periods, and the 6-min volume scans provided excellent temporal resolution of this development. For both cases, the 140 km × 180 km analysis domain covered the entire eastern dual-Doppler lobe (Fig. 2). This domain is over the High Plains well to the east of the Rocky Mountains, with a mean elevation about the same as the radars, about 1500 m. A detrimental aspect of this large-area emphasis is that vertical resolution becomes very degraded at maximum ranges: the beamwidth exceeds 2.5 km, the lowest 2.5 km AGL lies completely below the lowest beam center, and sampling through the entire storm depth is limited to as few as four or five scans. However, most of the analysis is at more favorable, better resolved ranges, and our focus on midlevel mesoscale motions makes the degraded resolution at far ranges more acceptable than if the focus was on convective scales.

Data processing relied on the well-known software packages RDSS, SPRINT, and CEDRIC (Oye and Carbone 1981; Miller et al. 1986; Mohr et al. 1986, respectively) developed at NCAR. Reflectivity and radial velocity data for each radar were edited and unfolded in radar coordinates and interpolated to a Cartesian grid over this domain, from 2.5 km MSL (~1 km AGL) to 15 km MSL, with horizontal and vertical grid spacing of 1.5 and 0.5 km, respectively. Other details of the dual-Doppler synthesis procedure are nearly identical to those described in Nachamkin et al. (1994). Important aspects to note here are that horizontal wind components were filtered so that features smaller than  $4\Delta x$  (6 km) were strongly damped and that the iterative derivation of the wind components accounted for particle fall speed (assuming ice and liquid, respectively, above and below

the freezing level of 4.85 km in both cases) and utilized a downward integration of the continuity equation for deriving vertical motion. Upward integration and variational techniques were not suitable due to a deep unsampled surface-based layer over much of the domain.

Many of the dual-Doppler results are presented as time–height cross sections, based on vertical profiles of horizontally averaged or areally integrated variables at each analysis time, over the several-hour analysis period, with no temporal smoothing. This method effectively averages out much of the convective-scale variability within the system, as well as random error. Remaining are important aspects of mesoscale evolution, as resolved from 23 dual-Doppler analyses at nominal 12-min intervals in the first case, and from 10 analyses at  $\leq 24$ -min intervals in the second case. Such time–height analyses are made over the entire MCS echo and separately over its convective and stratiform portions, where that distinction is based on threshold values of vertically integrated liquid water (VIL).

The precipitation analyses for the two MCSs were performed in slightly different ways as discussed later, but were both derived from gridded reflectivity fields with methods used by MC92. The Marshall–Palmer relation was used to convert reflectivity  $Z$  to rain rate  $R$  (a reflectivity–liquid water concentration relation based on the same assumptions was used in calculating VIL). No attempt was made to improve estimates of  $R$  with rain gauge data or with alternate  $Z$ – $R$  relations that may be more suitable (particularly for convection). As discussed by MC92, however, random error in  $R$  is largely eliminated in its areal integration over the echoes of interest to derive volumetric rain rate  $V$ , and despite remaining biases in  $V$ , trends in its time series reliably indicate mesoscale intensity trends of the MCS.

### 3. Analysis of 11–12 August 1992 MCS

#### a. System overview

A small MCS developed in northeastern Colorado during the late afternoon of 11 August 1992. The Denver sounding at 0000 UTC 12 August (Fig. 3; all times UTC; LST is 7 h earlier) shows light to moderate northwesterly flow up to 400 mb, with stronger westerlies aloft. This region was between a broad 500-mb ridge (trough) over western (eastern) North America and was approximately 800 km southwest of the polar jet maximum. Midlevels had moistened since the morning sounding, due to advected moisture from weak midday convection over the mountains. A weak front associated with the trough moved southward through the central plains a day earlier and stalled near the mountain–plains interface through Colorado into Wyoming. Surface flow on the High Plains was southeasterly upslope behind the front.

On the 11 August, conventional surface analyses indicate that a trough formed within the cool airmass,

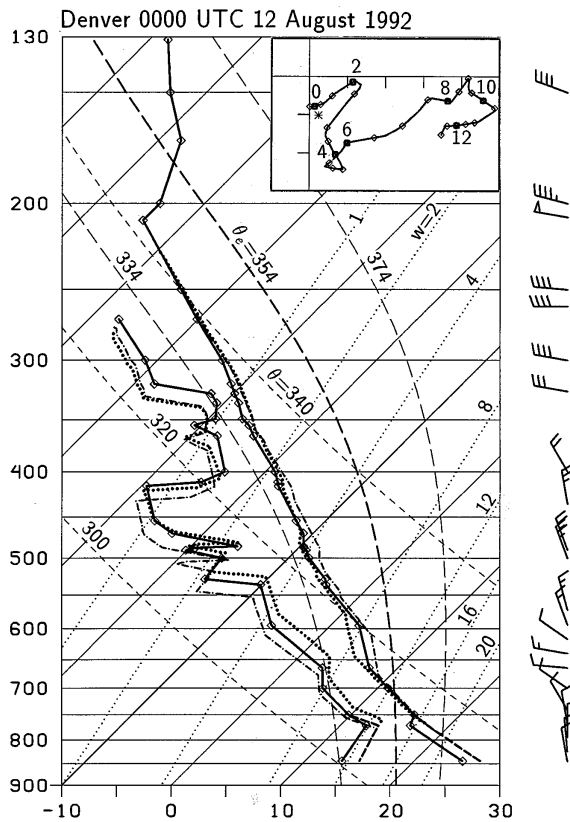


FIG. 3. Skew  $T$ - $\log p$  diagram for Denver sounding at 0000 UTC 12 August 1992. Temperature and dewpoint profiles include original sounding (solid lines connecting indicated mandatory and significant level data); a modified boundary layer ( $\theta_e = 354$  K) below 770 mb (dashed); an altered sounding (section 5c) due to deep tropospheric descent (dash-dotted); and an altered sounding due to low- to mid-level ascent and mid- to upper-level descent (dotted). Wind barbs indicate reported winds (barb— $5 \text{ m s}^{-1}$ ). Hodograph origin is  $(u, v) = (0, 0)$ ; tick mark interval is  $5 \text{ m s}^{-1}$ . Winds are indicated (labeled) every 0.5-km (2-km) AGL (station elevation 1611 m). Asterisk indicates storm motion.

extending northeastward from east of Denver across western Nebraska. Conventional surface and mesonet winds on the plains (sites in Fig. 2) were southeasterly to the southeast of this trough and were northerly or northeasterly to the northwest. The sounding in Fig. 3 was within these low-level northerlies. Values of  $\theta_e \geq 354$  K were observed on both sides of the surface trough. Parcels lifted from the modified boundary layer ( $\theta_e = 354$  K) in Fig. 3 produce a convective available potential energy (CAPE) of  $2315 \text{ J kg}^{-1}$ .

Deep convection initiated in northeastern Colorado well east of the high terrain. Several isolated cumulonimbi originated over a large area, probably aided by broad convergence associated with the surface trough but not in any apparent alignment with it. Infrared (IR) satellite imagery shows that the individual anvils of this widespread convection consolidated into a small but unified MCS (system A) by 0131 (Figs. 4a–c). During this development, adjacent convective activity weak-

ened over the mountains to the west and over the Palmer Divide to the south, leaving system A and another small MCS well to the south as the only significant convective activity in Colorado.

Radar shows that the initial widespread convection consolidated into four multicell clusters by 0029 (Fig. 5b); these are individually apparent in the concurrent IR image as well (Fig. 4b). These clusters retained their identities through and beyond the development of the unified MCS cloud shield (Figs. 5c,d). While the westernmost cluster weakened and later reintensified as a separate entity (Figs. 4e,f and 5e,f), the remaining clusters gradually consolidated into a single dominant cluster, which persisted past the last dual-Doppler analysis at 0353. After system A moved southeastward out of the analysis area, it eventually merged into the west flank of intensifying convection in northwestern Kansas (Fig. 4f), which developed into a larger MCS that dominated nocturnal convection over the plains.

Individual cell movement was generally to the south or southeast during system A's evolution, with new cells occasionally developing on the western flanks of the multicell clusters. Overall MCS motion was determined to be from  $347^\circ$  at  $5.2 \text{ m s}^{-1}$ . While all of its significant convection was within the dual-Doppler lobe throughout the analysis period, some of the upper-level anvil (Fig. 4) and associated stratiform echo (Fig. 5) advected beyond the eastern edge of the analysis domain.

### b. Precipitation evolution

Dual-Doppler analyses were performed for 23 volume scans over a 4.6-h period from 2317 to 0353. These are at nominal 12-min intervals, with two slightly longer intervals due to power and equipment failures. The precipitation analysis for system A is derived from the full sequence of reflectivity fields in these analyses, where each gridded value is the maximum from either radar. To avoid underestimation of VIL at ranges where the lowest one or more grid levels were unobserved (below the beam center of either radar's lowest scan), the reflectivity value (including no-echo) at the lowest observed level in a column was extended down to the first level. These fields were converted to rain-rate and liquid water concentration fields, and VIL was calculated over the depth of the analysis domain.

The total volumetric rain-rate ( $V_T$ ) time series for system A (excluding the non-MCS echo in Fig. 5) and for its convective and stratiform components ( $V_C$  and  $V_S$ , respectively) are shown in Fig. 6. These are based on rain-rate fields at 4-km MSL and on a convective–stratiform VIL threshold of  $2.5 \text{ kg m}^{-2}$ . Comparison with time series derived at other lower-tropospheric levels, using alternate VIL thresholds or comparable reflectivity thresholds (i.e.,  $\sim 35 \text{ dBZ}$ ) for convective–stratiform classification, or based on different  $Z$ - $R$  relations, showed little effect on their trends. Since relatively little stratiform echo developed in this case, the convective

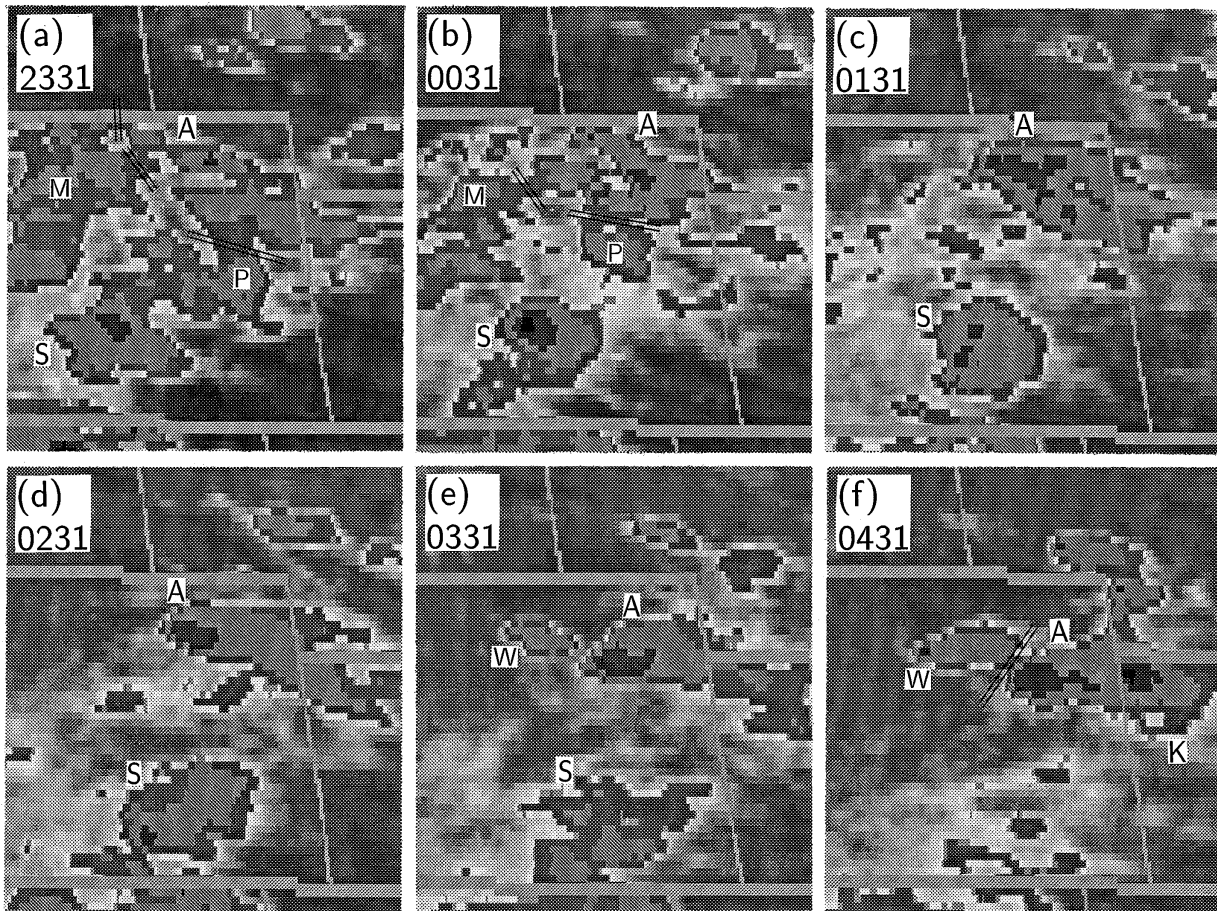


FIG. 4. IR satellite images for 11–12 August 1992 at UTC times (a) 2331, (b) 0031, (c) 0131, (d) 0231, (e) 0331, and (f) 0431. Each image is centered on eastern Colorado (state boundaries are shown) and is approximately 500-km east–west by 650-km north–south. IR temperatures of colder cloud tops are indicated by step-shading colder than  $-33^{\circ}\text{C}$  (medium gray),  $-43^{\circ}\text{C}$  (light gray),  $-54^{\circ}\text{C}$  (dark gray), and  $-60^{\circ}\text{C}$  (black). Continuous dark to white background ranges from cloud-free surface temperatures to cloud-top radiances of  $-32^{\circ}\text{C}$ . Short double line segments separate the small MCS of interest, system A, from other cloudiness discussed in text: M, over mountains; P, Palmer Divide; S, southern Colorado; W, west of system A; and K, northwestern Kansas.

component dominated the precipitation, so that  $V_C$  and  $V_T$  had almost identical trends throughout the 4.6-h period. After an explosive development beginning at 2341 (Fig. 5a),  $V_C$  quickly reached its maximum at 0029 (Fig. 5b), with an unsteady decrease to a minimum at 0217;  $V_C$  then increased again to 0305 and remained steady for the rest of the analysis period.

The system's convection could be grouped into several clusters that maintained identities for 1 h or more. In Fig. 5 these components are grouped into upshear and downshear ensembles, and the precipitation evolution of each ensemble was analyzed individually (Fig. 6). Both ensembles began intensifying rapidly before 0000. The downshear ensemble ( $C_D$ ) peaked 36 min prior to the upshear ensemble's ( $C_U$ ) maximum, and they weakened (unsteadily for the upshear component) to near-concurrent minima at about 0217. The MCS's reintensification after 0217 was seen in both ensembles before they consolidated and continued as a unified convective cluster.

Thus, system-wide evolution in  $V_C$  was due to component convective clusters that were somewhat in phase, as was observed by MC92 in several MCCs.

In order to eliminate finescale temporal variability, while retaining system-wide, meso- $\beta$ -scale trends, the  $V_C$  time series in Fig. 6 was smoothed with the same filtering procedure used by MC92. Although the magnitude of the smoothed time series is almost an order of magnitude less than the average  $V_C$  found in the developing stages of MCCs (Fig. 1), the overall trend in system A is similar: it intensifies rapidly to a meso- $\beta$  convective maximum (at 0038), decreases to a meso- $\beta$  minimum (at 0229), and reintensifies into a modest mature stage. Although some stratiform echo advected beyond the analysis domain, the lack of development of a significant stratiform component  $V_S$  in Fig. 6 is largely due to the minimal scale of the consolidated MCS, combined with evaporation of precipitation in the unsaturated layer beneath the anvil.

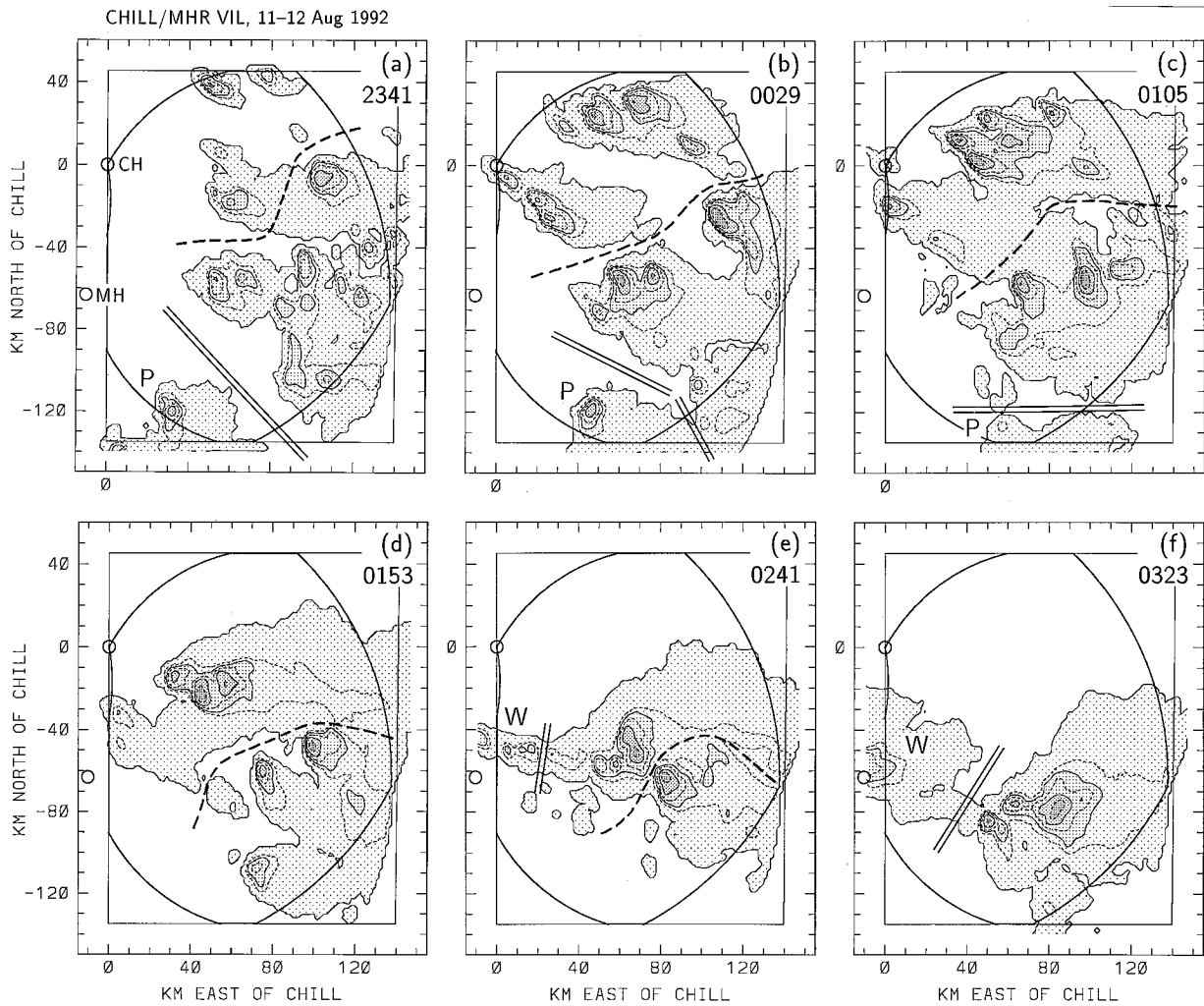


FIG. 5. Combined CHILL–MHR VIL maps of system A on 11–12 August 1992 at UTC times (a) 2341, (b) 0029, (c) 0105, (d) 0153, (e) 0241, and (f) 0323. Radar locations, dual-Doppler lobe and analysis domain are as in Fig. 2. Alternating solid and dashed VIL contours are 0.001, 0.333, 1.0, 3, 9, and 27  $\text{kg m}^{-2}$ . Progressively darker shading is thresholded by 0.001, 1.0, 9, and 27  $\text{kg m}^{-2}$ . Double line segments separate system A from echo associated with other cloudiness (labeled as in Fig. 4). Heavy dashed line in (a)–(e) divides system A into upshear and downshear portions (to the northwest and southeast, respectively).

### c. Kinematic evolution

Examples of dual-Doppler analyses are shown at 6-km MSL for 0053 and 0253 in Fig. 7. The first time is near the time of the meso- $\beta$  convective maximum (Fig. 6), well before the consolidation of the several convective clusters. The later time is during the re-growth period after the meso- $\beta$  minimum and after their consolidation. Average storm-relative winds derived at this level were northwesterly at these times and throughout the 4.6-h analysis period. Below this level they veered from southerly or southeasterly at the surface to westerly at 5 km MSL and above 8 km the northwesterlies backed to westerlies at 10 km. Vertical velocity ( $w$ ) patterns and magnitudes were reasonable for multicellular convection. Maximum  $w$  in the domain occurred in a number of different cells through the period,

occurred at mid- to upper levels, ranged from 9 to 27  $\text{m s}^{-1}$  for individual volume scans and correlated strongly with convective volumetric rain rate  $V_C$  in Fig. 6. Minimum  $w$  occurred at low to midlevels and ranged from  $-8$  to  $-18 \text{ m s}^{-1}$ .

Time–height cross sections of horizontally averaged or integrated kinematic variables provide a convenient method of analyzing the system-wide MCS evolution as a function of height over the analysis period. Such analyses are restricted to regions within the analysis lobe that have echo and radial winds reliably observed by both radars. A time–height section of the areal extent of derived winds is shown in Fig. 8a. Just as echo was partitioned in the precipitation analysis, winds in an entire column are considered to be in convective or stratiform regions depending on the VIL value for that

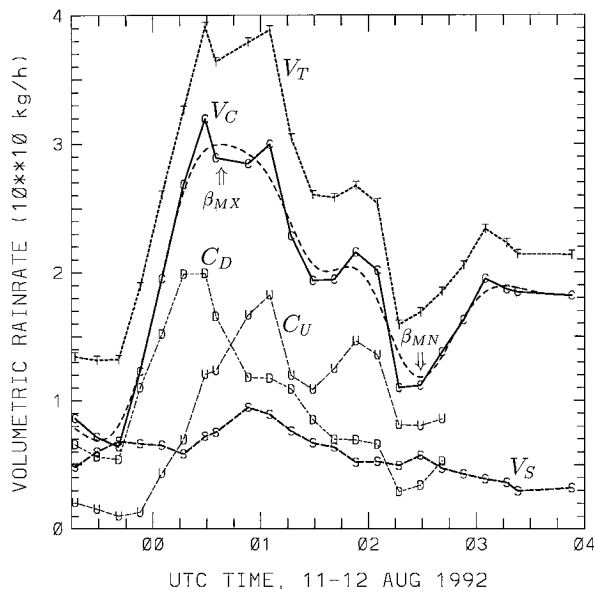


FIG. 6. Time series of volumetric rain rates in system A on 11-12 August 1992 for convective, stratiform, and total echo (heavy curves  $V_C$ ,  $V_S$ , and  $V_T$ , respectively). Convective curve  $V_C$  is partitioned into contributions by upshear and downshear clusters in Fig. 5 (thin curves  $C_U$  and  $C_D$ , respectively). Subscript labels along each curve denote radar observation times. The meso- $\beta$ -scale convective cycle (labeled  $\beta_{MX}$  and  $\beta_{MN}$ ) is defined by filtered  $V_C$  time series (unlabeled heavy dashed curve).

column; the partitioning in Figs. 8b,c is based on a threshold of  $2.5 \text{ kg m}^{-2}$ . The number of points used at a given level in the following kinematic analyses is the area in Fig. 8 divided by the  $2.25\text{-km}^2$  gridpoint area.

The stratiform area (Fig. 8c) dominates the total area pattern; the maximum, from 6 to 9 km MSL, is within and below the anvil, and the initial decrease below the maximum is due to evaporation of precipitation. In comparison, the smaller maximum area in convective regions (Fig. 8b) is fairly constant through a much deeper layer. The sharp decrease in both regions below about 4.5 km is due primarily to the unobserved layer beneath the lowest scans and to lesser extents is due to further evaporation of precipitation and the deletion of low-level data contaminated by ground clutter and other artifacts. Temporally, the maximum convective area correlates well with  $V_C$  in Fig. 6 through the meso- $\beta$  convective cycle and regrowth. The maximum stratiform area, at 0129, lags the meso- $\beta$  convective maximum and is generated largely by convective outflow aloft during that intense convection. This area gradually diminishes thereafter as system A consolidated into a very small MCS, with some of its stratiform echo advected eastward beyond the analysis domain (Fig. 5).

The horizontally averaged divergence evolution in system A is shown in Fig. 9a. With the loss of observed winds at low levels (Fig. 8), much of the actual surface-

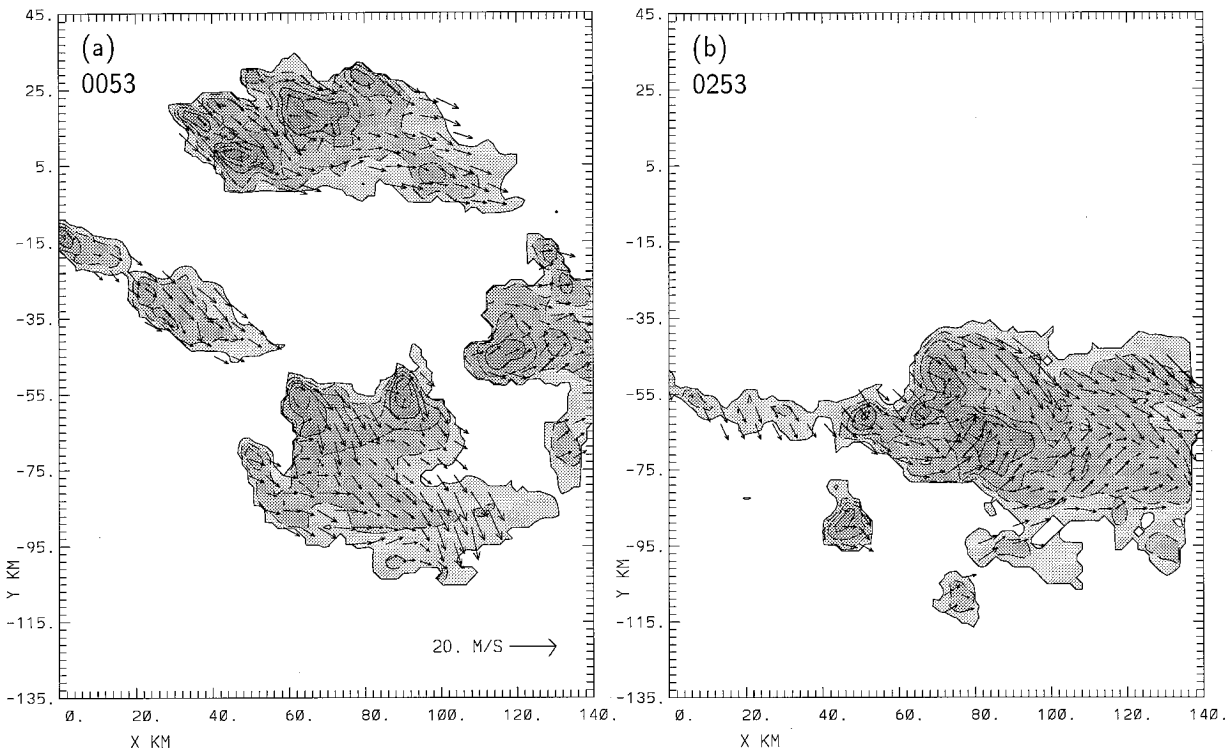


FIG. 7. Dual-Doppler analysis of system A on 12 August 1992 at (a) 0053 and (b) 0253 UTC. Reflectivity and storm-relative horizontal winds at 6 km MSL are shown. Contours and progressively darker shading are at 10-dBZ intervals beginning at 10 dBZ. Every third wind vector along  $x$  and  $y$  is depicted. Vectors are scaled  $10 \text{ m s}^{-1}$  per 6-km distance.

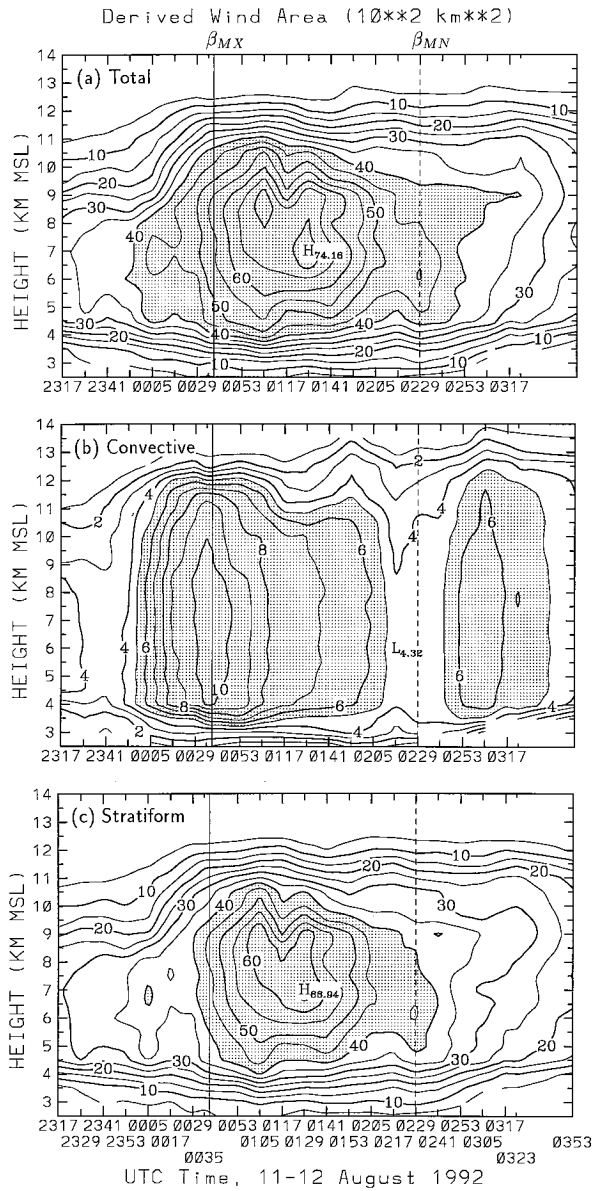


FIG. 8. Time-height cross sections of horizontal area  $A$  of dual-Doppler winds in system A on 11–12 August 1992. (a) Total area, (b) convective area, and (c) stratiform area. Units are  $10^2 \text{ km}^2$ . In (a) and (c) contour interval is 5 and  $A > 40$  is shaded. In (b) interval is 1 and  $A > 5$  is shaded. Individual analysis times are at tickmarks; all times are labeled in (c). Solid and dashed vertical lines labeled  $\beta_{MX}$  and  $\beta_{MN}$ , respectively, denote meso- $\beta$  convective cycle identified in Fig. 6.

based convergence into convection, as well as divergent outflow beneath downdrafts, is not included. Similarly, relatively few points above 12 km MSL may yield unrepresentative averages. Levels between approximately 4.5 and 12 km MSL are more reliably represented. Through the first half of the analysis period, mean convergence predominates at low to midlevels, with the level of nondivergence averaging about 6.5 km. After

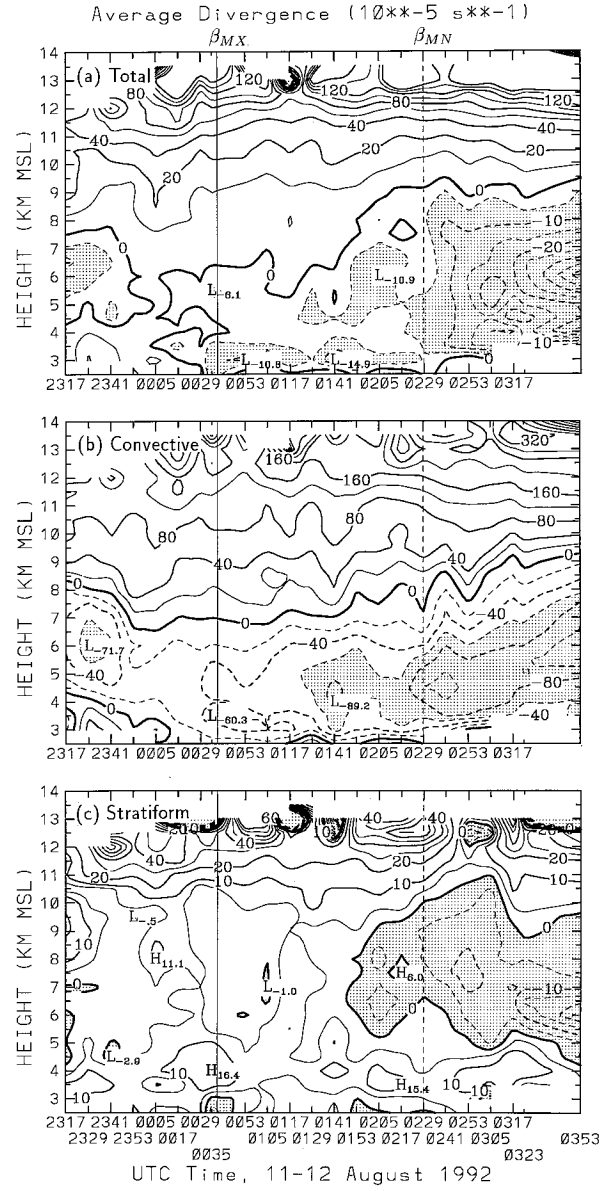


FIG. 9. Time-height cross sections of areally averaged horizontal divergence  $D$  in system A for (a) total, (b) convective, and (c) stratiform regions. Units are  $10^{-5} \text{ s}^{-1}$ . Positive (negative) contours are solid (dashed). In (a) contour intervals are 5 for  $D < 0$ , 10 for  $0 < D < 20$ , and 20 for  $D > 20$ . In (b) intervals are 20 for  $D < 40$  and 40 for  $D > 40$ . In (c) intervals are 5 for  $D < 10$ , and 10 for  $D > 10$ . Shading denotes (a)  $D < -5$ , (b)  $D < -60$ , and (c)  $D < 0$ . Other details are as in Fig. 8.

0141, mean convergence strengthens and deepens to 9.0 km. In the convective regions (Fig. 9b), mean divergence magnitudes (positive and negative) are considerably larger, the convergence layer in the lower troposphere is better defined, and the level of nondivergence does not increase as sharply, relative to the system-wide section in Fig. 9a. In the larger stratiform region (Fig. 9c), average divergence magnitudes are much smaller and upper-level divergence is the predominant

signal through the first half of the period. After 0141, a deep layer of midlevel convergence develops, which explains the sharp increase in the system-wide level of nondivergence in Fig. 9a. It should be stressed that this mean evolution may not be representative of any particular portion of the MCS. For instance, divergence and  $w$  profiles averaged over a particular cell are dependent on its life-cycle stage, and midlevel convergence for individual columns through sloped flow branches in a stratiform region is generally stronger but restricted to shallower layers than in Fig. 9c.

The vertical mass flux analyses are based on the Doppler-derived vertical motion fields and an approximate density profile that decreases exponentially with height. System-wide mass flux (Fig. 10a) is generally upward, implying that a comparable amount of compensating downward mass flux is occurring outside detectable echo. The level of maximum flux rises from about 6.5 km MSL during the first half of the period to 9.0 km during the latter half. Mass flux in the convective regions (Fig. 10b) dominates the system-wide flux. The mid- to upper-level maximum correlates well in time with the convective rain rate  $V_c$  in Fig. 6. In particular, the maximum mass flux at 0035 is associated with the meso- $\beta$  convective maximum in  $V_c$ , the minimum in mass flux (at 0217) coincides with the meso- $\beta$  minimum, and the subsequent increase toward the second largest maximum flux at 0305 occurs with the regrowth in  $V_c$  after the meso- $\beta$  cycle. During this regrowth, the level of maximum flux in the convective region lifts from 7.0 to 8.5 km, and downward mass flux develops in low levels. In stratiform regions (Fig. 10c), generally weak upward mass flux is seen through the first half of the period. After 0141, a deep midlevel layer of downward flux develops, coincident with the onset of deep midlevel convergence in the stratiform region (Fig. 9c), and general upward mass flux remains in upper levels.

These analyses indicate that several characteristic features of mature MCSs developed rather abruptly after about 0141. System-wide, the level of nondivergence, and the level of maximum net upward mass flux (and mean vertical motion), rose by several kilometers and net downward mass flux developed in low to midlevels. These changes are most evident in the stratiform region. Moreover, these kinematic signatures of mature stage structure appear on the order of an hour following a meso- $\beta$  convective precipitation maximum (Fig. 6), consistent with the generalized scenario hypothesized by MC92. Note that these time-height analyses appear somewhat noisy. Some of this is due to real convective variability; for example, the maximum convective flux at 0141 in Fig. 10b is associated with the secondary precipitation maximum by the upwind cluster at 0153 in Fig. 6. Some of the variability may be due to limitations imposed by the long baseline in resolving convective circulations in this marginal-sized MCS. However, the meso- $\beta$ -scale trends indicating upscale evo-

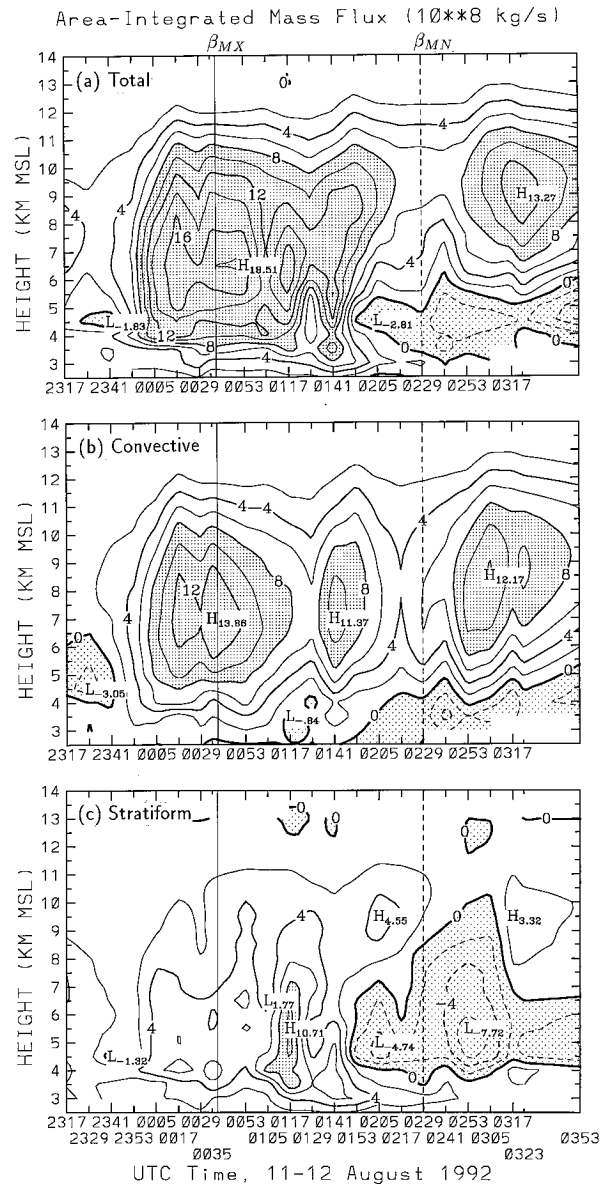


FIG. 10. Time-height cross sections of areally integrated vertical mass flux MF in system A for (a) total, (b) convective, and (c) stratiform regions. Units are  $10^8 \text{ kg s}^{-1}$ . Positive contours are solid and negative contours are dashed. Contour interval is 2; MF < 0 is shaded lightly; MF > 8 is shaded darker. Other details are as in Fig. 8.

lution are not too obscured by such small-scale variability.

Recall that the system-wide meso- $\beta$  convective cycle resulted from individually evolving upshear and downshear clusters that were somewhat in phase. Time-height sections of average divergence and vertical mass flux for each of these components (not shown) indicate the same signatures of mature-stage structure developing at almost the same time (after 0141), well before their consolidation into a single large cluster (Fig. 5d). This concurrent, similar evolution in the component

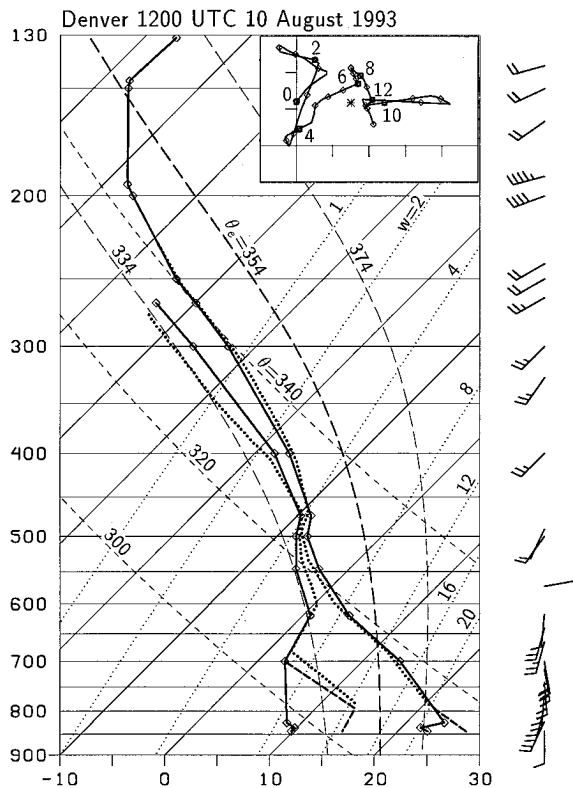


FIG. 11. Skew  $T$ -log $p$  diagram for Denver sounding at 1200 UTC 10 August 1993. Temperature and dewpoint profiles include original sounding (solid); modified boundary layer ( $\theta_e = 354$  K) below 795 mb (dashed); and an altered sounding due to low- to midlevel ascent and mid- to upper-level descent (dotted). Other details are as in Fig. 3.

clusters suggests that it was modulated by mesoscale convective dynamics on the scale of the entire ensemble. In particular, the upscale evolution appears to be an ensemble-scale response, with about a 1-h lag, to the thermal forcing associated with the meso- $\beta$  convective maximum. After examining a slightly larger MCS with more typical structure in the next section, the nature of the linkage between the forcing and upscale evolution will be investigated.

#### 4. Analysis of 10–11 August 1993 MCS

##### a. System overview

The second case occurred a year later on the afternoon of 10 August 1993. The Colorado “monsoon” environment was well defined, with relatively barotropic conditions, a maximum CAPE of about  $2095 \text{ J kg}^{-1}$  (based on boundary layer  $\theta_e$  of 354 K), and deep moist southerly to southwesterly winds (Fig. 11). Convection was widespread but much was weak and capped by a stable layer near 500 mb. A series of MCSs (Fig. 12) began unusually early in the diurnal cycle, forced in part by a short wave propagating across Colorado from the southwest. Systems A, B, C, and D developed in

succession in northeastern Colorado, tracked northeastward, and dissipated over Nebraska. Each system was a little larger and longer-lived than its predecessor. System SE developed in southeastern Colorado and continued its growth into a nocturnal MCC over Kansas.

Because of the extensive areal coverage of these systems, long-range surveillance scans from MHR were used for the reflectivity overview and precipitation analysis. Scans at  $0.5^\circ$ ,  $1.2^\circ$ , and  $2.5^\circ$  and out to 318 km were gridded onto a single level at 5 km AGL, at a horizontal grid spacing of 3 km, using the REORDER software package described by Oye and Case (1992). The radar sequence in Fig. 13 shows that system C was particularly well observed for 3 h as it developed and matured in the eastern dual-Doppler lobe.

System C’s initial convection developed from 1900 to 2000 in higher terrain about 50 km southwest of MHR. It developed along an axis that extended northeastward into the dual-Doppler domain and into the southwest flank of the weakening system B. Convection in system C (Figs. 12a, 13a) was concentrated in two meso- $\beta$ -scale entities: a quasi-stationary cluster 30–40 km south of MHR, and an intensifying cluster 60 km east of MHR that was merged into the southwest flank of system B. System C’s continued growth (Figs. 12b,c) was centered on the eastern cluster, which developed into a north–south convective line that propagated eastward through the dual-Doppler lobe (Figs. 13b–d). An extensive stratiform echo developed to the north and west of the line, with the MCS echo assuming an asymmetric leading line–trailing stratiform configuration (Houze et al. 1990) by 2330.

This configuration was not very persistent, however, as the convective line continued to propagate southeastward into an area of weaker, preexisting convection to the south and east of the analysis domain (Figs. 13d–f). The convective ensemble, after propagating almost completely away from the stratiform echo of system C that it had spawned, redeveloped into the next distinct MCS in the series, system D (Figs. 12d–f). While the convection moved beyond the analysis domain during this evolution, system C’s stratiform echo remained dynamically active and in coverage for some time before moving northeastward out of range. Mean system motion was determined to be from  $232^\circ$  at  $9.5 \text{ m s}^{-1}$ .

##### b. Precipitation evolution

The precipitation analysis for system C (Fig. 14) was carried out with long-range reflectivity fields from MHR at 12-min intervals. Insufficient data were available for deriving VIL over this large area, so instead several reflectivity thresholds were used to distinguish convective from stratiform echo; the components in Fig. 14 are based on a 38-dBZ threshold. The rapid succession of MCSs and widespread, weaker convection on this day made it difficult to unambiguously include or exclude some echo with system C. The primary curves

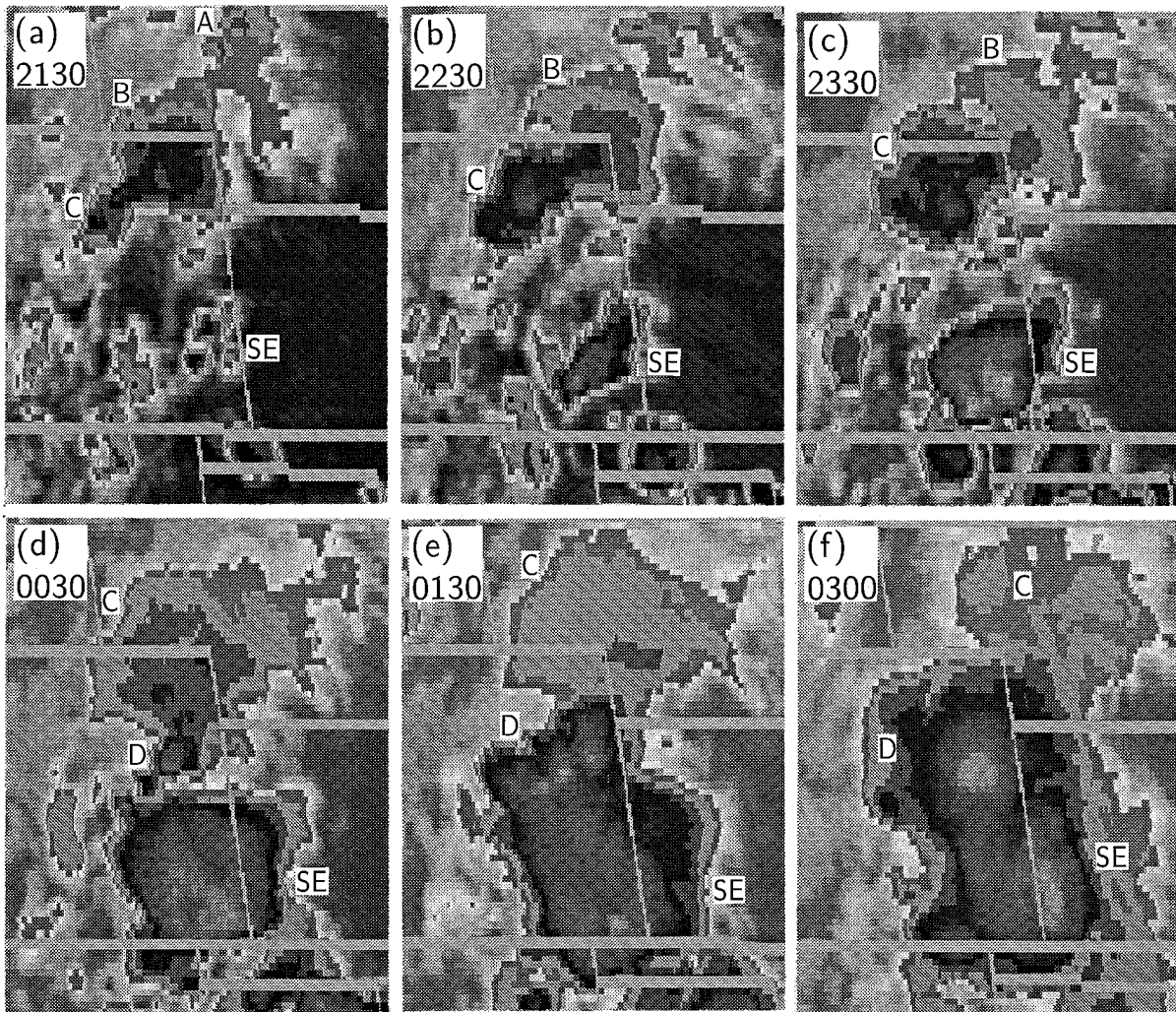


FIG. 12. The IR satellite images for 10–11 August 1993 at UTC times (a) 2130, (b) 2230, (c) 2330, (d) 0030, (e) 0130, and (f) 0300. Each image is centered on eastern Colorado (state boundaries are shown) and is approximately 500-km east–west by 750-km north–south. IR temperature shading is as in Fig. 4; interior dark to light shading indicates colder cloud tops in this case, from  $-63^{\circ}\text{C}$  to about  $-75^{\circ}\text{C}$ . Labels refer to MCSs described in text. System C is the primary MCS of interest.

( $V_T$ ,  $V_C$ , and  $V_S$ ) are based on a liberal inclusion of echo, including the early convection that bridges systems B and C in Figs. 12a and 13a, and the later convection that propagates southeastward out of system C and redevelops into system D. Also included are system B's remnants after 2216 as it weakens at far range (Fig. 13b), and the bands of the weaker, capped echo that extend southwestward to higher terrain.

As in the previous case, the time series for this slightly larger MCS resemble the generalized MCC curves in Fig. 1, though they are still only one-third to one-half of the magnitude seen in the developing stages there. In particular, the convective component  $V_C$  displays a well-defined meso- $\beta$  convective cycle. Its filtered time series shows a sharp increase to a meso- $\beta$  maximum at 2159, a decrease to a minimum at 2307, and then re-intensification for about an hour as the system matures.

The time series labeled  $C_2$  in Fig. 14 is based on a more conservative definition of system C's convective ensemble and is seen to dominate the more liberally defined  $V_C$  curve. The curve  $C_2$  is the sum of those labeled  $C_M$  and  $C_Q$ , which are for the quasi-stationary convective cluster south of MHR in Fig. 13 and for the cluster farther east that develops into the squall line, respectively. These two clusters intensify and weaken in phase and together produce the meso- $\beta$  convective cycle. The system-wide increase in  $V_C$  after the meso- $\beta$  minimum is due primarily to the squall line. Although its initial regrowth after 2300 was clearly within system C for some time, it gradually became disassociated with system C and by 0030 was responsible for the developing system D (Figs. 12c–e and 13c–f). The  $V_C$  curve and the analysis of system D become unreliable after 0000 due to the range of this convection from MHR and

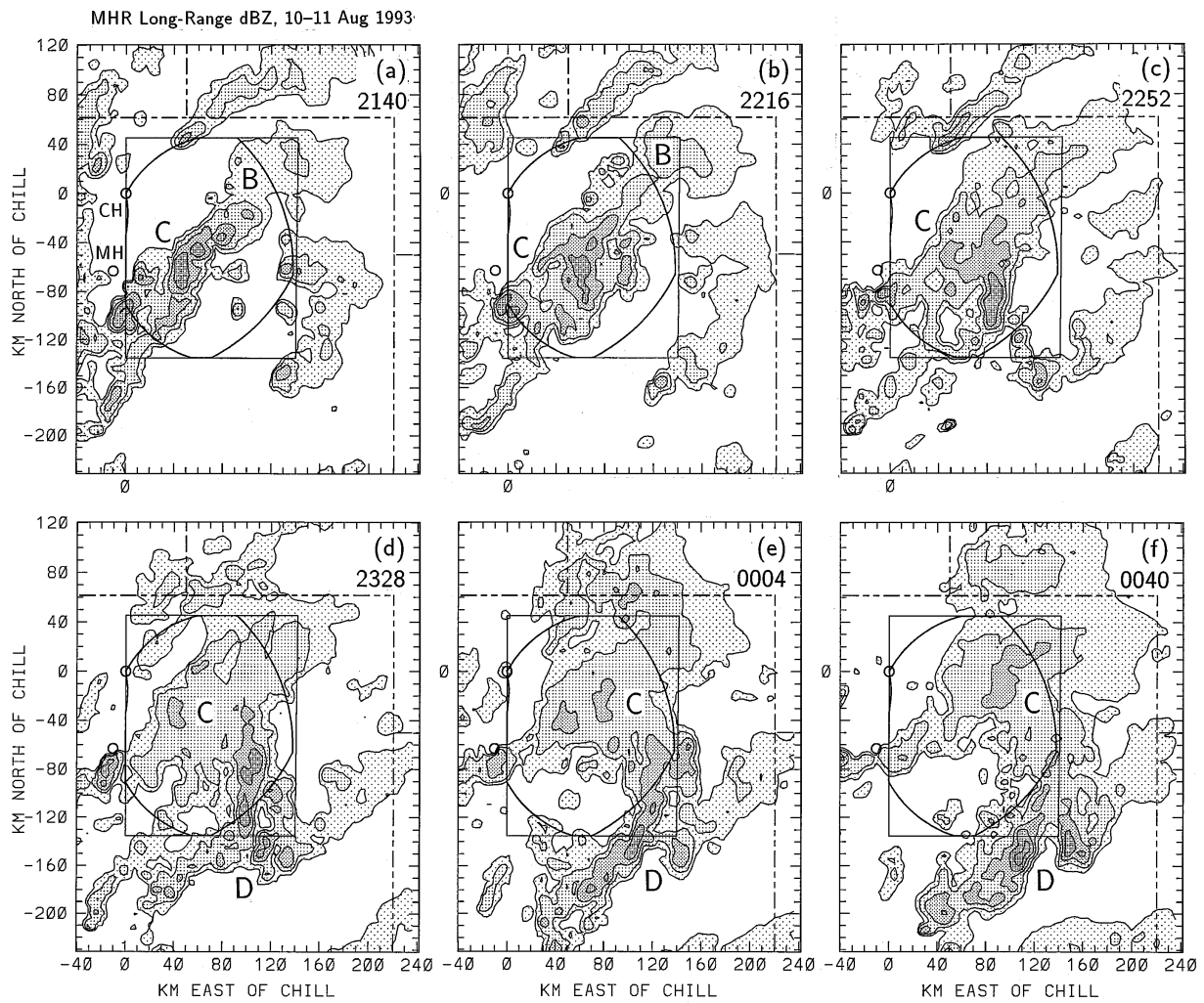


FIG. 13. MHR long-range reflectivity maps of system C on 10–11 August 1993 at UTC times (a) 2140, (b) 2216, (c) 2252, (d) 2328, (e) 0004, and (f) 0040. Radar locations, dual-Doppler lobe and analysis domain are as in Fig. 2. Contours and progressively darker shades begin at 15 dBZ and are at 10-dBZ intervals. Labeled echoes are associated with the corresponding cloud shields in Fig. 12.

possible attenuation by the convection just to the south-east of MHR (Fig. 13e).

A significant stratiform component  $V_s$  developed in this MCS. The growth of  $V_s$  through 2300 is fairly steady, with the large jumps from 2128 to 2140 and from 2216 to 2228 due to the stepwise inclusion of preexisting echo into system C. However, the increased growth rate in  $V_s$  beginning at the meso- $\beta$  convective minimum near 2300 resembles the generalized trend in Fig. 1 and is due to an increase in area and intensity of a typical, asymmetrically trailing stratiform echo (Houze et al. 1990).

### c. Kinematic evolution

Ten dual-Doppler analyses were performed over a 2.4-h period from 2159 to 0023, beginning near the meso- $\beta$  convective maximum in  $V_c$ . These are at 24-min intervals, with 6-min intervals during the critical upscale

evolution stage from 2247 to 2305. Example analyses (Fig. 15) at 2223 and 2359, at 5 km MSL, indicate a developing flow structure typical of MCSs with leading line–trailing stratiform structure (e.g., Houze et al. 1989).

At 2223 (Fig. 15a), shortly after the meso- $\beta$  maximum, the dominant convective cluster was near the center of the domain and developing into a north–south line. By 2359 (Fig. 15b), the convective line had developed southward and propagated almost completely out of the analysis lobe (Fig. 13e) and the asymmetric, trailing stratiform region had become much more extensive. Ahead (east) of this convection, strong relative low-level inflow was evident throughout the period, veering from easterly at the lowest observed levels to southeasterly at 5 km. This is the typical front-to-rear flow branch, which ascended through the convective region and continued rearward and northward into the trailing stratiform region in mid- to upper levels. By

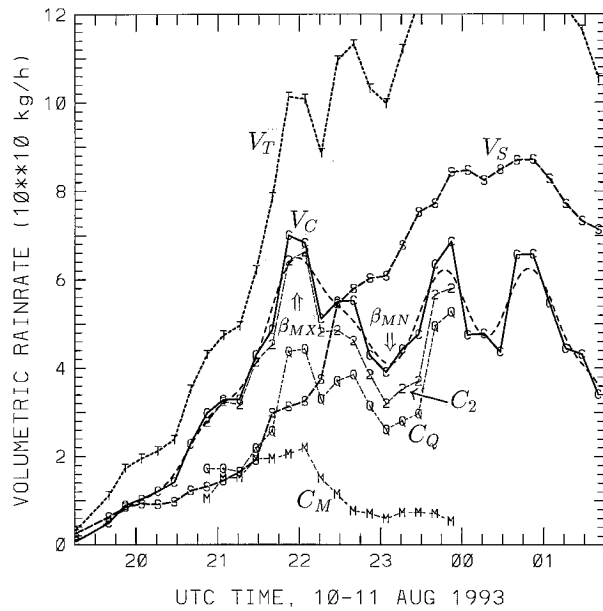


FIG. 14. Time series of volumetric rain rates in system C on 10–11 August 1993, for convective, stratiform, and total echo (heavy curves  $V_C$ ,  $V_S$ , and  $V_T$ , respectively), based on liberal inclusion of echo. Thin curve  $C_2$  is convective volumetric rate based on a more conservative definition of system C and is the sum of contributions by the cluster south of MHR and the squall-like cluster further east in Fig. 13 (thin curves  $C_M$  and  $C_Q$ , respectively). Other details are as in Fig. 6.

2359, this branch had developed well north of the convective line and was providing easterly inflow directly into the predominantly stratiform region. Strong cyclonic vorticity just south of the terminus of this organized easterly inflow [near  $(x, y) = (88, -45)$ ] marks a feature similar to the cyclonic member of the “book-end” vortices simulated by Weisman (1993) and observed by Scott and Rutledge (1995). Using slightly different storm motions, a closed vortex with diameter 20–30 km could be identified through the last hour. Beneath the front-to-rear flow in the stratiform region, a midlevel rear inflow branch just beginning to develop at 2223 became stronger and much more extensive by 2359. Also evident at the later time is weak midlevel inflow into the northern and southern flanks of the stratiform region.

The quasi-stationary convective cluster south of MHR (Fig. 13) was too near the baseline for complete dual-Doppler analysis, and flow associated with it (e.g., from  $x = 0$  to 20 km and  $y = -105$  to  $-65$  km in Fig. 15a) is excluded from the following kinematic analyses. While this cluster was significant in the initial stages (curve  $C_M$  in Fig. 14), it soon weakened and became relatively insignificant. The remaining area of derived winds (Fig. 16a) shows an upper-level maximum at 10–11 km MSL through most of the period. This is much higher than the maximum for the previous case (Fig. 8a), probably due to both a higher equilibrium level and weaker upper-level flow in this case (Figs. 11, 3). The

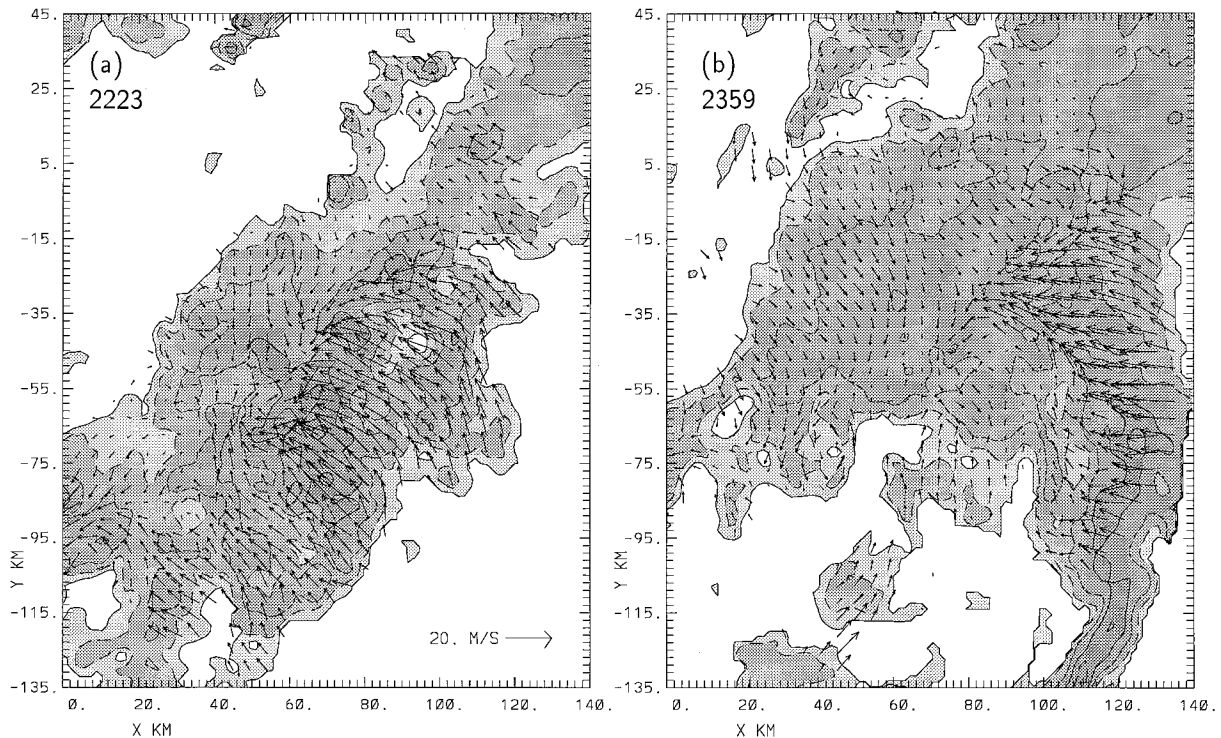


FIG. 15. Dual-Doppler analysis of system C on 10 August 1993 at (a) 2223 and (b) 2359 UTC. Reflectivity and storm-relative horizontal winds at 5 km MSL are shown. Contours and vectors are as in Fig. 7.

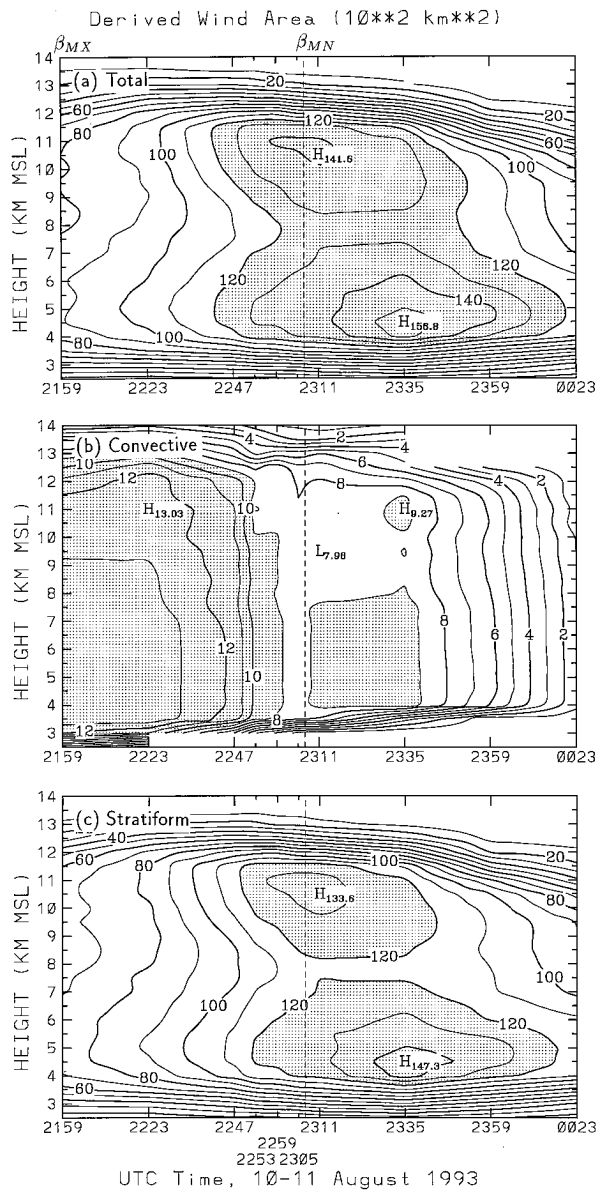


FIG. 16. Time-height cross sections of area  $A$  of dual-Doppler winds in system C on 10–11 August 1993. (a) Total area, (b) convective area, and (c) stratiform area; units are  $10^2 \text{ km}^2$ . In (a) and (c) contour interval is 10 and  $A > 120$  is shaded. In (b) contour interval is 1 and  $A > 9$  is shaded. Meso- $\beta$  convective cycle (with  $\beta_{MX}$  at initial time 2159) is identified in Fig. 14. Other details are as in Fig. 8.

maximum extent of these upper-level winds is attained midway through the period, about an hour after the meso- $\beta$  convective maximum. Another maximum occurs throughout the period at 4.5–5.0 km, due to the shallower bands of echo that are capped by the midlevel stable layer. As in the previous case, system-wide kinematic analysis at low levels becomes increasingly incomplete with decreasing height (below 4.0 km MSL in this case) and most of the winds were in the stratiform region (Fig. 16c). Maximum area in the convective re-

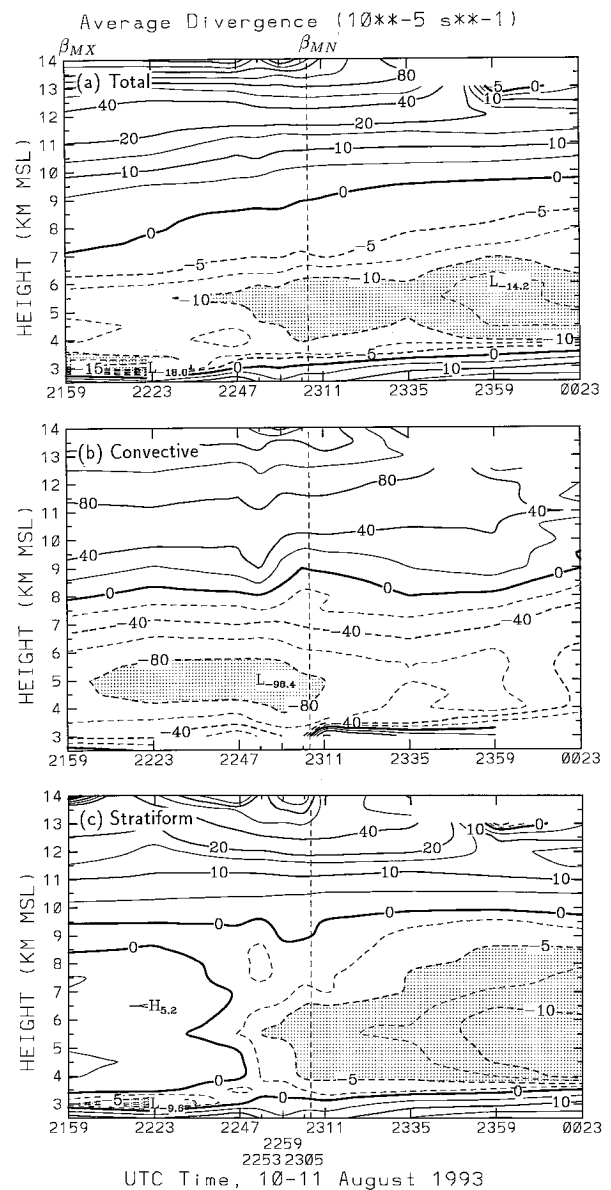


FIG. 17. Time-height cross sections of divergence  $D$  in system C for (a) total, (b) convective, and (c) stratiform regions. Units are  $10^{-5} \text{ s}^{-1}$ . Positive (negative) contours are solid (dashed). In (a) contour intervals are 2.5 for  $D < -5$ , 5 for  $-5 < D < 20$ , and 20 for  $D > 20$ . In (b) intervals are 20 for  $D < 40$  and 40 for  $D > 40$ . In (c) intervals are 2.5 for  $D < 0$ , 5 for  $0 < D < 20$ , and 20 for  $D > 20$ . Shading denotes (a)  $D < -10$ , (b)  $D < -80$ , and (c)  $D < -5$ . Other details are as in Fig. 16.

gion occurred early at 2159, and a temporal minimum occurred at 2305, coinciding with the meso- $\beta$  convective cycle of  $V_C$  in Fig. 14. Convective area subsequently increased with the regrowth in  $V_C$  but after 2335 the convection exited the analysis lobe fairly quickly.

System-wide average divergence (Fig. 17a), as in the previous case, shows midlevel convergence strengthening and deepening into higher levels in the hour following the meso- $\beta$  convective maximum. In the con-

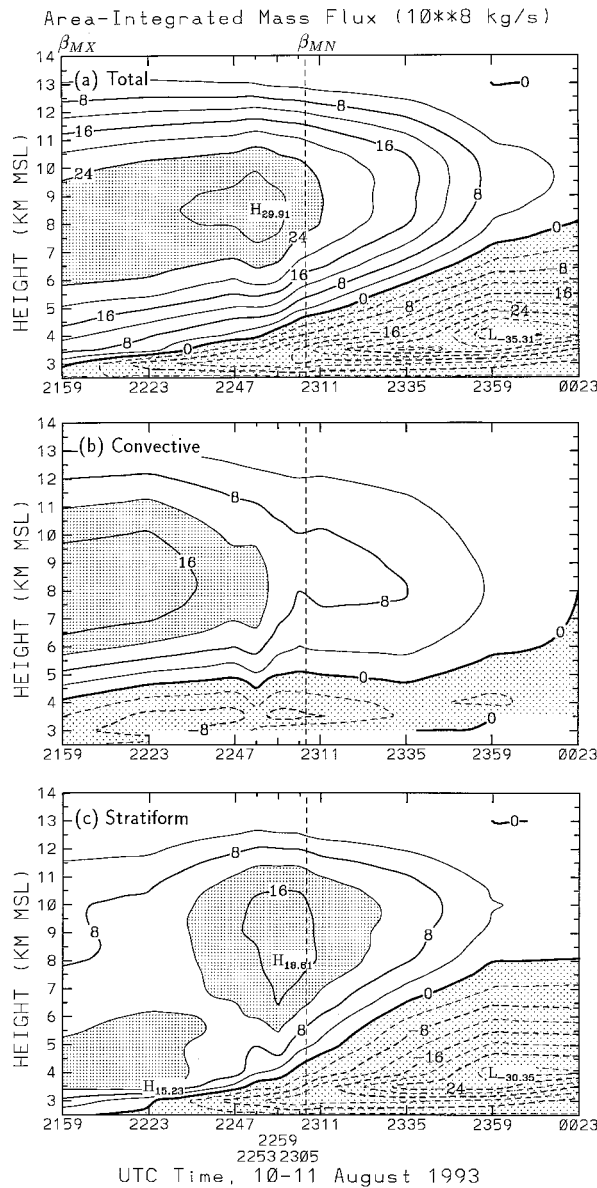


FIG. 18. Time-height cross sections of vertical mass flux MF in system C for (a) total, (b) convective, and (c) stratiform regions. Units are  $10^8 \text{ kg s}^{-1}$ . Positive contours are solid and negative contours are dashed;  $\text{MF} < 0$  is shaded lightly. Contour interval is 4. Medium shading denotes (a)  $\text{MF} > 24$  and (b),(c)  $\text{MF} > 12$ . Other details are as in Fig. 16.

vective region (Fig. 17b), stronger midlevel convergence centered at 5 km MSL becomes most intense in the first hour and then gradually weakens in the last hour as the convection leaves the domain. Thus, most of the system-wide evolution is occurring in the stratiform region (Fig. 17c), where deep midlevel convergence begins by 2247 and strengthens over the following hour.

There is smoother, more continuous evolution of total mass flux for system C (Fig. 18a) than in the previous

case. A predominantly upward flux through most of the troposphere for the first hour is dominated initially by upward mass flux in the convective region (Fig. 18b), and then by the development of strong mid- to upper-level flux in the stratiform region (Fig. 18c) as the convective flux diminished. Unlike the previous case, any subsequent increase in upward flux that was likely associated with the regrowth in  $V_c$  after the meso- $\beta$  cycle was not detected, due to the convection leaving the lobe. System-wide, lower-tropospheric downward mass flux continuously deepens and strengthens throughout the period. Again, this evolution is dominated initially by the convective region for the first hour, where downdrafts in heavy precipitation are predominant in the lowest levels. By 2247, however, the rapid development of a deepening downward flux in the stratiform region dominates the systemwide evolution.

In summary, system C displayed kinematic evolution consistent with a maturing MCS, such as a deepening level of nondivergence and the development of low- to midlevel downward mass flux. These changes were most pronounced in the stratiform region, where they developed more abruptly about an hour after the meso- $\beta$  convective maximum. While system C resembled a leading-line, asymmetrically trailing-stratiform structure in the classification scheme of Houze et al. (1990), these changes and their temporal relation with the meso- $\beta$  cycle are similar to those seen in the smaller, less classifiable MCS in section 3. Moreover, this kinematic evolution is consistent with the generalized upscale evolution scenario for MCSs that was hypothesized by MC92. The dynamic linkage between the meso- $\beta$  convective cycle and the subsequent upscale evolution is examined next.

### 5. Linearized response to the meso- $\beta$ convective cycle

#### a. The linearized model

Nicholls et al. (1991; hereafter NPC91) developed analytic solutions for the linearized response of a simplified hydrostatic atmosphere, initially at rest, to prescribed localized heating. For a 2D incompressible atmosphere with a rigid lid at 10 km, they described the space- and time-dependent responses to a constant heat source and to “pulse forcing,” in which constant heating stops after 2 h. For both constant and pulse heating, they considered a heating rate magnitude  $Q_{m0} = 2 \text{ J kg}^{-1} \text{ s}^{-1}$ , vertically distributed in an  $n = 1$  (or  $n1$ ) mode (Fig. 19a). The half-sine wave gives symmetric, positive-only heating with a maximum at 5 km. When distributed also symmetrically in the horizontal as in Fig. 19b (half-width  $a = 10 \text{ km}$ ), this  $n1$  heat source represents the first-order effect of latent heating by localized deep convection (about  $30 \text{ mm h}^{-1}$  over a 20-km width). NPC91 also considered a constant heat source with both  $n1$  and  $n2$  modes (Fig. 19a). The  $n2$  mode’s full-sine wave pro-

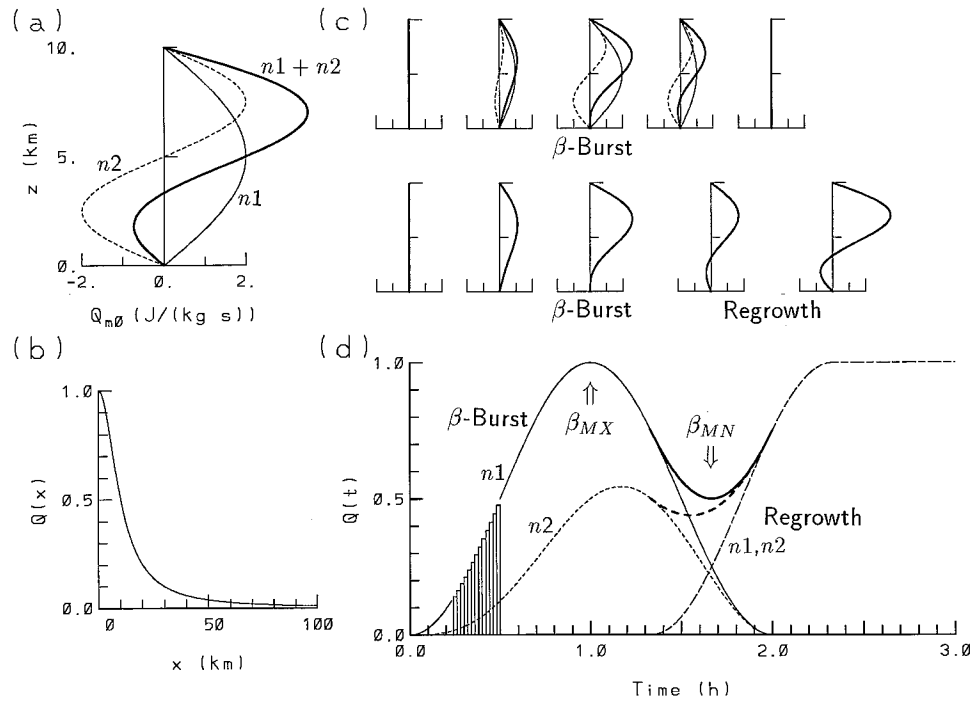


FIG. 19. Thermal forcing specifications for the linearized model. (a) Vertical distribution of maximum heating rate magnitude  $Q_{m0}$  for  $n1$  mode (thin solid),  $n2$  mode (thin dashed), and  $n1 + n2$  modes (heavy solid). (b) Horizontal dependence factor  $Q(x)$  on heating profiles in (a). (c) Time-dependent heating profiles at  $x = 0$  for several times along time axis in (d). Limits of axes are as in (a). Top row: profiles for meso- $\beta$  convective burst with  $n1$  mode (thin solid) and  $n1 + n2$  modes (heavy solid); contribution of  $n2$  mode is shown (thin dashed). Bottom row: profiles for meso- $\beta$  burst followed by regrowth, due to  $n1 + n2$  modes. (d) Time-dependence factor  $Q(t)$  on heating profiles in (a). For the meso- $\beta$  burst (0–2 h), factors for  $n1$  mode (thin solid) and, when included,  $n2$  mode (short dashed) are shown. For the meso- $\beta$  burst followed by regrowth (beginning at 1.33 h), the  $n1 + n2$  burst is used, and regrowth factors are identical for  $n1$  and  $n2$  modes (thin long dashed). Overlapping period from 1.33 to 2.0 h shows added factors from the two heating phases for  $n1$  (heavy solid) and  $n2$  (heavy dashed) modes. Combined  $n1$  curve defines meso- $\beta$  maximum and minimum. Thin bars following  $n1$  curve from 0.25 to 0.5 h illustrate a series of short-duration, constant-amplitude heat pulses used to build the time-dependent heating.

vides equal magnitudes of heating aloft and low-level cooling (no net heating). When superimposed on the  $n1$  mode using the same  $Q_{m0}$ , the asymmetric total heating profile resembles that seen in an MCS: maximum heating is stronger and shifts upward, and low-level cooling of weaker magnitude represents net evaporation in lower levels. Despite limitations of this idealized model, Bretherton and Smolarkiewicz (1989), NPC91, Pandya et al. (1993), and Mapes (1993) have shown such analytic solutions capture many features of thermally forced gravity waves that have been simulated in more complex models.

NPC91 suggested that the response to more complicated heating specifications could be made by considering a series of pulses, where the response to each pulse is additive in the linearized model. That approach is taken here to specify time-varying heating profiles that approximate the meso- $\beta$  convective cycle and reintensification as in Fig. 1. As will be shown, the linearized response in the region containing the heating is temporally consistent with the observed kinematic evolu-

tion described in sections 3 and 4. The response to a rapidly intensifying convective ensemble is shown to act as a self-modulating mechanism that helps explain the observed meso- $\beta$  convective cycle and associated upscale evolution.

Two approximations of the meso- $\beta$  convective burst are considered. The simplest contains only the  $n1$  mode. Its maximum amplitude  $Q_{m0}$  varies in time by a sine-squared factor over a half period from time  $t = 0$  to 2 h, with maximum heating at 1 h (Figs. 19c,d). This represents the rapid growth of convection and subsequent weakening that produces the meso- $\beta$  convective maximum of precipitation in Fig. 1.

A more realistic approximation of the meso- $\beta$  burst is made by adding an  $n2$  mode to the  $n1$  forcing. The full-amplitude  $n2$  mode is modulated by the same sine-squared factor, multiplied by an additional factor that varies linearly from 0 to 1 over the same 2 h. The resulting  $n2$  amplitude (Figs. 19c,d) approaches but remains less than the  $n1$  amplitude (unlike NPC91's equal  $n1$  and  $n2$  forcing) during this early stage because of

the predominance of convective over stratiform processes; however, increasing relative  $n_2$  amplitude accounts for increasing influence by a developing stratiform region. The smaller  $n_2$  amplitude is similar to the  $n_1 + n_2$  forcing considered by Mapes (1993), who showed that the important effects of the  $n_2$  mode occur even with no net low-level cooling (e.g., at  $t = 1$  h in Fig. 19c). To the extent that low-level cooling might be more associated with convective than stratiform rain during this stage, note that the  $n_2$  maximum lags the  $n_1$  maximum by  $\sim 10$  min, which is comparable to the microphysical and hydrometeor fallout timescale associated with maximum condensation in convection and subsequent low-level evaporational cooling.

A third scenario involves regrowth of the system following the meso- $\beta$  convective burst. The regrowth contains  $n_1$  and  $n_2$  modes, both modulated identically by a sine-squared factor over a quarter-wave period beginning at  $t = 1.33$  h and reaching a steady maximum at  $t = 2.33$  h (Fig. 19d). When considered with the meso- $\beta$  burst containing  $n_1$  and  $n_2$  modes, the net heating profile varies as shown in the second row of Fig. 19c. The superimposed  $n_1$  modes from the meso- $\beta$  burst and regrowth produce a meso- $\beta$  cycle with a maximum and minimum at 1 h and 1.67 h, respectively, followed by reintensification to steady maximum heating at 2.33 h. The amplitude of the superimposed  $n_2$  modes equals the  $n_1$  amplitude by 2 h. This evolution approximates the meso- $\beta$  convective cycle and subsequent regrowth in Fig. 1, including the increasing influence of stratiform precipitation in a maturing MCS.

The prescribed heating for each of these modes and periods is built with a series of short-duration heat pulses that follow the time-dependent amplitude (e.g., Fig. 19d). The analytical solutions of NPC91 (for wind components  $u$  and  $w$ , pressure and buoyancy) apply to each short-duration pulse and are added to give the response to any of the prescribed heating scenarios as functions of  $(x, z, t)$ . These responses are first shown, for  $u$  and  $w$ , over a large, 500-km horizontal domain in order to compare with the results of NPC91. All variables used in the solutions are the same as used by them (e.g., buoyancy frequency, heating half-width, and constant density value) except  $Q_{m0} = 2 \text{ J kg}^{-1} \text{ s}^{-1}$  in all solutions here, whereas they halved this value in their solutions for  $n_1 + n_2$  forcing. As in NPC91, the heating is centered at  $x = 0$  and the response is symmetric in the  $x$  direction.

For the meso- $\beta$  burst with  $n_1$  forcing only, at  $t = 1$  h when heating is at its maximum, upper-level outflow from and low-level inflow into the heated region is seen (Fig. 20a). Strong upward motion is centered on the heating and much weaker compensating subsidence has developed out to  $x = 100$  km (Fig. 20b). At  $t = 2$  h (Figs. 20c,d), when heating ceases, the outflow-inflow branches and upward motion have decoupled from the heated region and are propagating outward as an  $n_1$  gravity wave roll. These solutions are very similar to those seen in NPC91 for  $n_1$  forcing (their Figs. 3a,b

and 10a,b). Because of the gradual buildup to maximum heating and gradual decline here, horizontal gradients of  $u$  and  $w$  are weaker, maxima are weaker, and the horizontal wavelength of the disturbance is shorter than given by the constant-amplitude 2-h pulse forcing in NPC91. However, the resultant  $n_1$  meso- $\beta$  gravity wave roll propagates at the same phase speed in both cases,  $31.8 \text{ m s}^{-1}$ .

The effects of adding the  $n_2$  mode into the meso- $\beta$  burst are evident in Figs. 20e,f at  $t = 2$  h. The  $n_2$  vertical structure is superimposed on the trailing half of the  $n_1$  gravity wave roll inside  $x = 100$  km. The overall structure can be compared to the solutions for constant  $n_1 + n_2$  forcing in NPC91 (their Figs. 5a,b) with differences again explained by the time-dependent heating here. By  $t = 4$  h (Figs. 20g,h), 2 h after the thermal forcing ends, both  $n_1$  and  $n_2$  gravity wave rolls have moved beyond  $x = 100$  km, and the  $n_1$  roll has completely outrun the  $n_2$  roll, which propagates half as fast.

Figures 20i,j show the added effects of the regrowth heating phase at  $t = 4$  h, well after it has reached its steady maximum. The inflow and outflow branches and vertical motion structure near the thermally forced region are similar to the constant  $n_1 + n_2$  forcing seen in NPC91 (their Figs. 5a,b) and resemble the kinematic structure of mature MCSs. The leading branches of the  $n_1$  and  $n_2$  gravity wave rolls from the regrowth heating phase are superimposed on the rolls produced by the meso- $\beta$  burst.

#### *b. Linearized response to prescribed meso- $\beta$ cycle and observed similarities*

The response in the meso- $\beta$ -scale region containing the prescribed heating is now examined, first for the meso- $\beta$  burst with  $n_1$  forcing only. Figures 21a,b show time-height cross sections of horizontal divergence (derived from analytic  $u$  fields) and vertical motion, respectively, horizontally averaged over  $x = 0$  to 50 km. Due to symmetry, this represents a 100-km-wide region centered on the thermal forcing. Mean upper-level divergence, low-level convergence, and upward motion develop and then weaken over the 3-h period, with maxima at 1.45 h, or 27 min after the meso- $\beta$  convective maximum. Averaged over a smaller, 0–20-km width (Figs. 21c,d), average divergence and  $w$  more than double, and the maxima occur only 13-min after the meso- $\beta$  maximum. This represents strong low-level convergence and upward motion in the “convective” region, which maximize as the forcing weakens and the  $n_1$  gravity wave roll begins to propagate away. In the near-environmental region from 20 to 50 km (Figs. 21e,f), there is initially low-level divergence and downward compensating subsidence, associated with the leading branch of the gravity wave roll. After the leading branch propagates beyond that region, low-level convergence and upward motion develop, with maxima about 45-min after maximum heating.

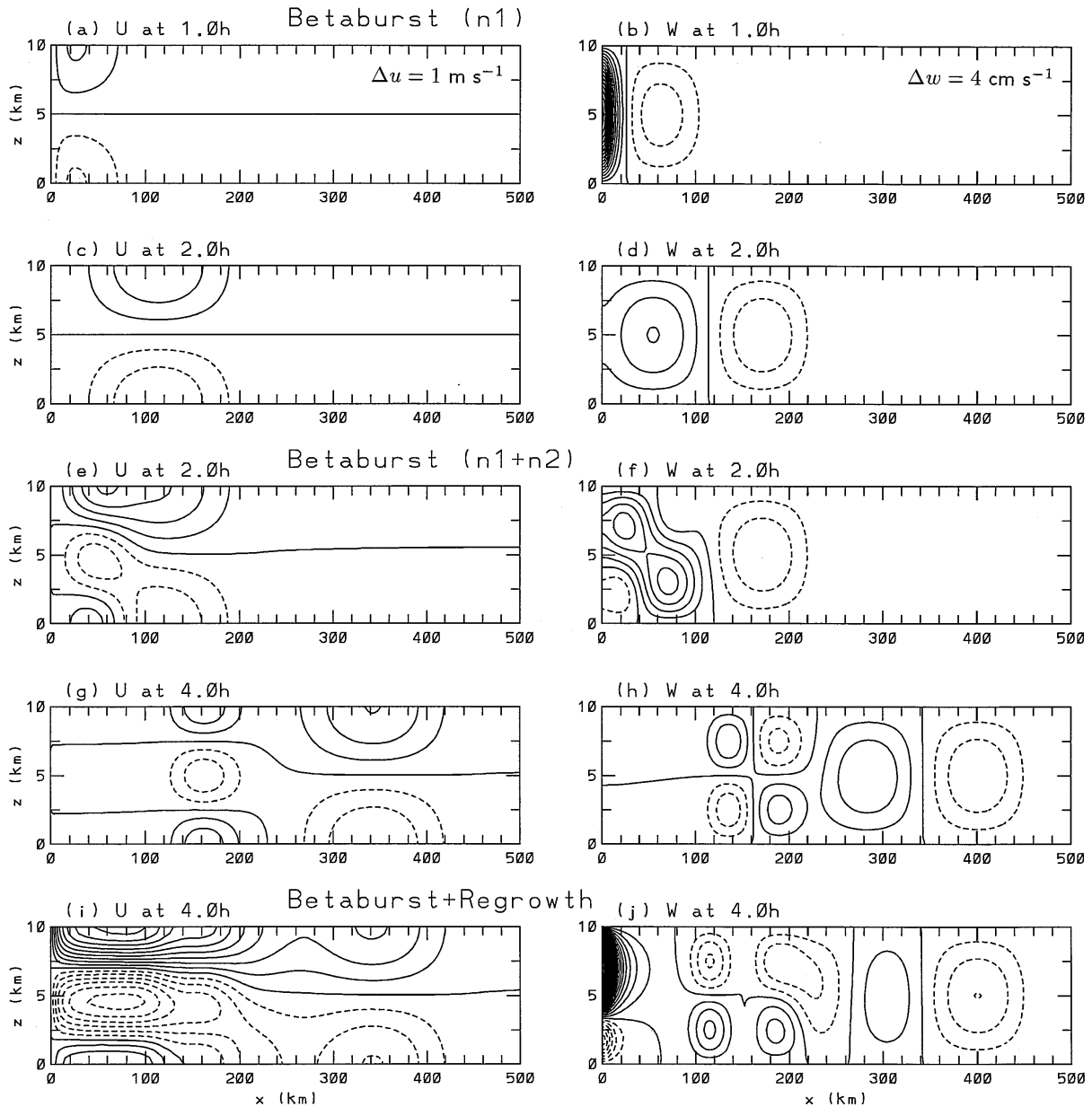


FIG. 20. Fields of  $u$  (left panels) and  $w$  (right panels), showing linearized response over large domain to three heating scenarios: meso- $\beta$  convective burst with  $n1$  forcing only, at (a),(b)  $t = 1.0$  h and (c),(d)  $t = 2.0$  h; meso- $\beta$  burst with  $n1 + n2$  forcing, at (e),(f)  $t = 2.0$  h and (g),(h)  $t = 4.0$  h; meso- $\beta$  burst and regrowth at (i),(j)  $t = 4.0$  h. Contour interval for  $u$  is  $1 \text{ m s}^{-1}$  and for  $w$  is  $4 \text{ cm s}^{-1}$ . Negative contours are dashed; zero and positive contours are solid.

The observed kinematic evolution in the MCSs described in sections 3 and 4 (despite the somewhat noisy appearance of the time-height plots for the first case) bears similarities to this first-order linearized response. In both cases, pronounced low- to midlevel, system-wide convergence developed during the hour following the meso- $\beta$  convective maximum. This convergence was stronger and developed earlier in the convective portions than in the stratiform echo (Figs. 9, 17). Similarly, strong upward mass flux predominated in the

MCSs through the hour following the meso- $\beta$  maximum, and the maximum flux in the convective area lagged the meso- $\beta$  maximum by a shorter time than did the maximum flux in the stratiform region (Figs. 10, 18).

In general, the magnitudes of the divergence extrema in the observed time-height analyses (excluding unreliable low and uppermost levels) are several times (up to an order of magnitude) greater than the extrema in the linear analyses. Observed extrema of average  $w$  (not

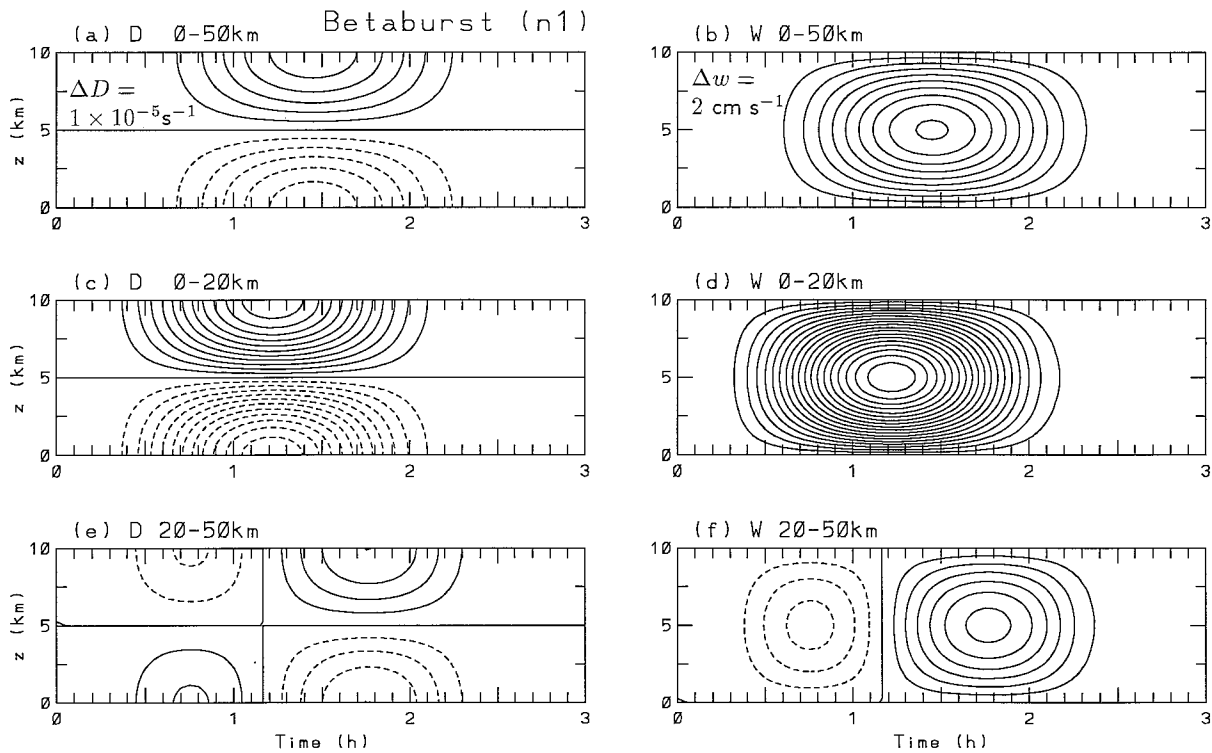


FIG. 21. Time-height cross sections of average horizontal divergence  $D$  (left panels) and  $w$  (right panels) over three averaging widths, showing evolving response to meso- $\beta$  convective burst with  $n1$  forcing. Average response over (a),(b) 0–50-km “total” region, (c),(d) 0–20-km “convective” region, and (e),(f) 20–50-km near-environmental region. Contour interval for  $D$  is  $1 \times 10^{-5} \text{ s}^{-1}$  and for  $w$  is  $2 \text{ cm s}^{-1}$ . Negative contours are dashed; zero and positive contours are solid.

shown, but their patterns are similar to the mass flux analyses) are greater than those in the linear solutions by similar factors. Several reasons could account for these differences. First, while NPC91 equated their net (2D integrated)  $n1$  heating to a reasonable convective rain rate of  $30 \text{ mm h}^{-1}$  over a 20-km width,<sup>1</sup> that neglects condensate storage aloft, or excess net condensation over precipitation. Through an MCS’s development, the storage rate can equal or exceed precipitation rate; to account for both the same rain rate and storage rate,  $Q_{m0}$  should be doubled or more, which would increase the linearized response proportionately. Second, the observations are restricted to echo and are thus biased toward more dynamic regions; the inclusion of intervening and adjacent no-echo regions in the horizontal averages would likely reduce the observed magnitudes. Third, whereas the model includes only the linearized response to prescribed heating, the observations include the nonlinear, nonhydrostatic dynamics (i.e., deep convection) that generate much of the diabatic heating, in addition

<sup>1</sup> An assumed length of 50 km for the 2D heating gives  $R = 30 \text{ mm h}^{-1}$  over  $1000 \text{ km}^2$ , and  $V = 3 \times 10^{10} \text{ kg h}^{-1}$ . These values are comparable to the maximum observed convective area and  $V_c$  in the first MCS (Figs. 8b, 6) and up to a factor of 2 smaller than those in the second MCS (Figs. 16b, 14).

to some approximation of the linearized response to that heating. Despite such uncertainties, similarities in the observed and model evolution suggest that the observational analyses reflect this linearized response.

For the linearized response to the meso- $\beta$  burst with both  $n1$  and  $n2$  modes, low-level convergence and mean upward motion begin to develop over the entire 0–50-km region (Figs. 22a,b) as with the  $n1$  forcing only. However, with the  $n2$  effects, strongest convergence shifts from low to midlevels in the hour after maximum heating, the convergence layer deepens to higher levels, and maximum  $w$  similarly shifts upward from 5 km. This response is stronger and occurs a little earlier over the 0–20-km “convective” region (Figs. 22c,d). Over the 20–50-km near-environment, the shift of surface convergence to midlevels and the corresponding upward shift of maximum  $w$  occur more abruptly at about  $t = 1.75 \text{ h}$  (Figs. 22e,f). The low-level cooling of the  $n2$  mode results in system-wide low-level divergence and downward motion by  $t = 2 \text{ h}$ . These features develop about 30 min later in the 20–50-km region than in the central region but with about the same magnitude.

Further similarities are seen between the observed evolution in both MCSs and the linearized response to this more realistic meso- $\beta$  burst. System-wide convergence strengthens at low levels soon after the meso- $\beta$

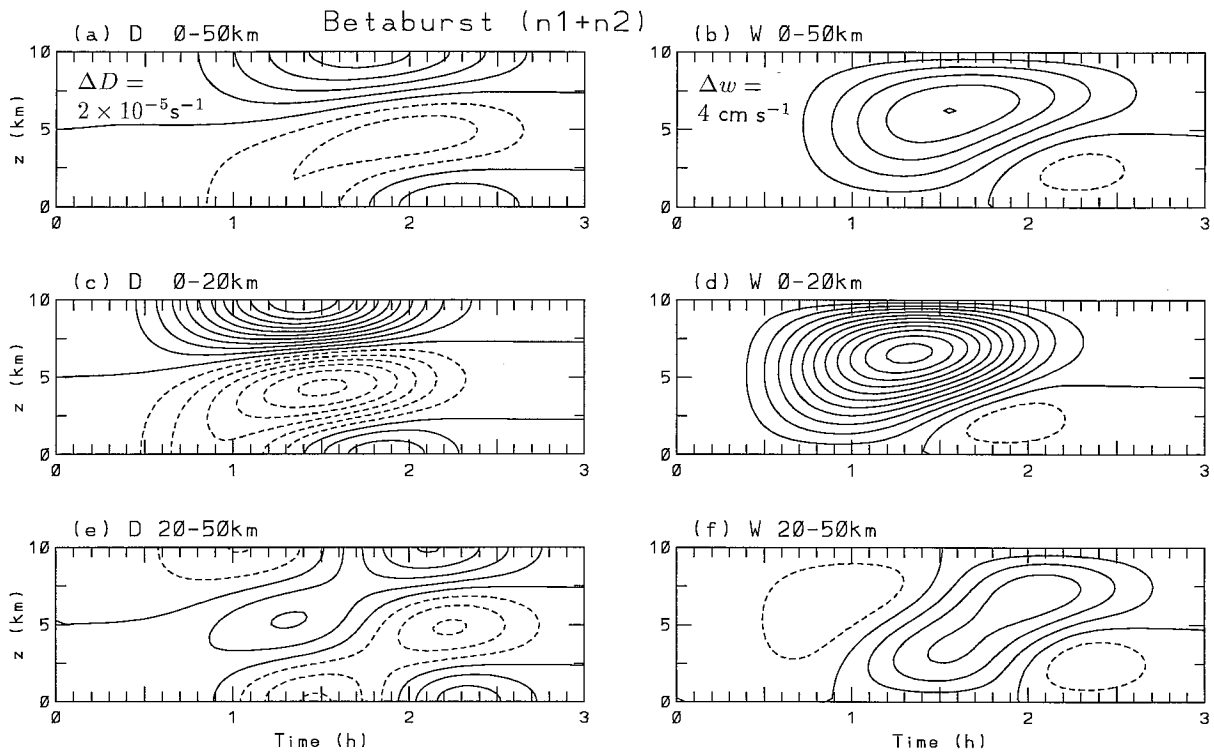


FIG. 22. Same as in Fig. 21 except showing response to meso- $\beta$  convective burst with  $n_1 + n_2$  forcing. Contour interval for  $D$  is  $2 \times 10^{-5} \text{ s}^{-1}$  and for  $w$  is  $4 \text{ cm s}^{-1}$ .

maximum, maximum convergence subsequently shifts upward to midlevels, and the overall convergence layer deepens appreciably (Figs. 9a, 17a). Similarly, maximum net upward mass flux shifts upward from midlevels following the meso- $\beta$  maximum, and net downward mass flux develops (or strengthens) in low levels (Figs. 10a, 18a). While the low-level divergence seen in the linearized response is hardly evident (especially in the first case), the mean low- to midlevel descent is more reliable due to the calculation of  $w$  by downward integration from better-observed regions aloft.

The observed strengthening of low-level convergence in the convective region after the meso- $\beta$  maximum (Figs. 9b, 17b) is similar to the linearized response in the 0–20-km region for both  $n_1$  and  $n_1 + n_2$  forcing (Figs. 21c, 22c). While the upward shift of convergence

(and of maximum  $w$ ) seen with the  $n_1 + n_2$  forcing was not observed in the convective region (possibly due to strong nonlinear effects), the  $n_1 + n_2$  effects in the 20–50-km region resemble those observed in the MCS stratiform regions. In particular, the abrupt development of midlevel convergence observed about an hour after the meso- $\beta$  maxima (Figs. 9c, 17c) resembles the midlevel convergence developing after  $t = 1.75 \text{ h}$  in Fig. 22e. Similarly, the linearized evolution of mean  $w$  in Fig. 22f is evident in Figs. 10c and 18c, where maximum upward mass flux shifts higher and a deep layer of downward flux develops.

For the 0–50-km averaged response to the third scenario, the meso- $\beta$  burst with  $n_1 + n_2$  forcing followed by regrowth, low-level convergence (Fig. 23a) sharpens after the meso- $\beta$  maximum, lifts to midlevels, and in-

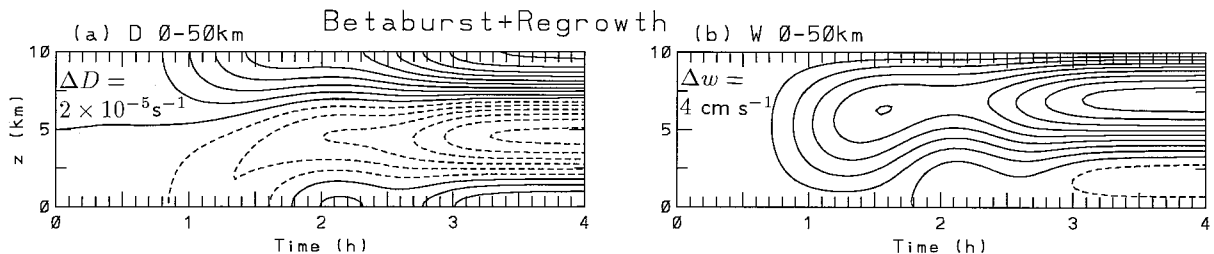


FIG. 23. Same as in Fig. 21 except showing response to meso- $\beta$  burst and regrowth over entire 0–50-km “total” region only. Contour interval for  $D$  is  $2 \times 10^{-5} \text{ s}^{-1}$  and for  $w$  is  $4 \text{ cm s}^{-1}$ . Time period is 1 h longer than in Figs. 21 and 22.

tensifies to a steady maximum. These tendencies are seen in the observed system-wide divergence evolution in Figs. 9a and 17a, where strong midlevel convergence is apparent through the end of the analyses. Average  $w$  in the linearized response (Fig. 23b) reaches a temporal maximum after the meso- $\beta$  maximum followed by reintensification to a steady maximum, with steady low- to midlevel descent developing. Similar evolution is seen in the observed system-wide mass flux analyses in Figs. 10a and 18a. However, there is no second maximum in the second case due to the reintensified convection leaving the analysis lobe.

*c. A positive feedback mechanism for MCS growth*

The observed kinematic evolution following an early meso- $\beta$  convective cycle in the two MCSs was shown to be similar to the linearized response to prescribed heating that approximates such a convective burst and its reintensification. This response is now examined further to show how it influences and may be partially responsible for that evolution.

First, given a rapidly intensifying convective ensemble in an environment favorable for MCSs, why is its early growth interrupted, thus yielding the meso- $\beta$  convective cycle? The initial response to the increased diabatic heating is deep compensating subsidence in the near environment (e.g., Fritsch 1975; Figs. 20b, 21f, 22f). As discussed by Tripoli and Cotton (1989a,b), this subsidence warming results in a local environment with reduced CAPE and thus acts as a self-braking mechanism on convective intensity.

This effect was applied to the sounding (with modified boundary layer) for the first MCS. The meso- $\beta$  burst with  $n1 + n2$  heating was used, and a column of parcels was initialized at 100 km and 1.8 h, when maximum subsidence due to the leading  $n1$  branch has occurred (just before the time of Fig. 20f). At this range the prescribed heating drops to less than 1% of central heating (Fig. 19b), and buoyancy and vertical displacement  $\Delta z$  are due almost totally to adiabatic perturbations on the basic state.<sup>2</sup> From the analytic  $u$  and  $w$  fields, back trajectories to  $t = 0$  were computed in order to find the original level and  $\Delta z$  for the parcels. From these calculations, the lowest 10 km of the sounding (the 10.5-km troposphere is only slightly deeper than the

<sup>2</sup> The same effects are seen much closer (i.e., the initial subsidence in Fig. 21f), but buoyancy perturbations and  $\Delta z$  become more influenced by local diabatic heating, especially inside 20 km. In convective ensembles, diabatic heating is much more concentrated in convective updrafts, and initial compensating subsidence occurs in the intervening and adjacent regions around the cells (e.g., Fritsch 1975) before propagating away from the heat source (Bretherton and Smolarkiewicz 1989). Thus, the suppressing effects of adiabatic subsidence should apply also to the immediate region containing the convection. The same reasoning applies to adiabatic motions induced by the  $n2$  mode.

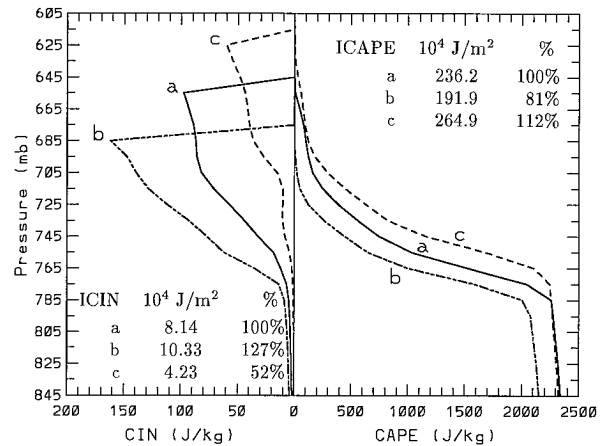


FIG. 24. Profiles of CAPE (right) and CIN (left; note different scales) for 10-mb thick mixed parcels, based on soundings in Fig. 3. Profiles: (a) observed sounding with modified boundary layer below 770 mb; (b) altered sounding due to deep tropospheric descent; and (c) altered sounding due to low- to midlevel ascent and mid- to upper-level descent. Insets give ICAPE and ICIN and their magnitude relative to sounding (a).

10-km model height) was displaced, conserving  $\theta$  and mixing ratio, to obtain a sounding affected by the deep subsidence (Fig. 3). Comparisons of CAPE and convective inhibition (CIN) profiles (Fig. 24) indicate that the suppressing effects of the  $n1$  mode are due to both a decrease in CAPE at all levels and a general increase of CIN. Integrated CAPE (ICAPE), as defined by Mapes (1993), is reduced to 81% of its original value. A corresponding quantity defined as integrated CIN (ICIN) increases to 127%.

Other factors that could cause this characteristic weakening after a meso- $\beta$  maximum are considered in section 6, but subsidence warming in response to the  $n1$  heating is considered here to be the most general mechanism that could suppress an entire convective ensemble simultaneously. Next, given this characteristic weakening after an initial rapid intensification phase, how does the ongoing linearized response favor the ensemble's reintensification and upscale growth? The trailing branch of the  $n1$  gravity wave roll restores the sounding back to its original state, but there is no further forced lifting that would be conducive to convection at any time with the  $n1$  heating only.<sup>3</sup> However, the ascent does remove the suppressing effects of the subsidence warming, and the low-level central region is supplied with relatively unaltered ambient air from further out (Figs. 20a,c). Thus, with any extra forcing focused on the central region, such as preexisting convergence that

<sup>3</sup> The stronger upward than downward motion seen in the 20–50-km region in Fig. 21f does result in final positive  $\Delta z$ , but this is proportional to local diabatic heating (negligible at far range) that would not occur in the no-echo regions adjacent to convection.

might help initiate a convective ensemble in the first place, the ensemble could reintensify.

The response to the meso- $\beta$  burst with  $n_1$  and  $n_2$  modes is more interesting in that it provides that extra forcing. There is a transient state where low-level parcels are forced above their equilibrium level (becoming negatively buoyant) before descending to their final level. Maximum displacement is reached after passage of the leading, low-level upward branch of the  $n_2$  gravity wave roll, that is, at about  $x = 40$  km at 2 h in Fig. 20f and at 160 km at 4 h in Fig. 20h. This upward branch is “compensating ascent” for the  $n_2$  mode’s thermally forced, low-level descent in the central region. The transient, negative buoyancy perturbation is then restored by the trailing low-level descent of the  $n_2$  roll.

Mapes (1993) identified important consequences of such boundary layer ascent resulting from heating scenarios similar to those considered by NPC91 (i.e., constant heating and “pulse forcing”). The ascent deepens the boundary layer, resulting in an increase of ICAPE. Also, the ascent destabilizes the lower atmosphere and allows convection to be triggered more easily. Although a contra-acting transient descent aloft stabilizes upper levels and reduces ICAPE, Mapes described how its negative influence on convection is marginal compared to the positive influences below. He argued that these thermally forced effects by an MCS favor additional deep convection in its mesoscale vicinity and thus help explain the gregarious nature of tropical convection.

The same reasoning is invoked here, on space and timescales closer to the parent ensemble than considered by Mapes (1993), to explain how these effects favor the upscale evolution of the parent convection into an organized MCS in the first place. The observed soundings were modified based on back trajectories from a column at 100 km and at 2.9 h, when maximum low-level lifting has occurred due to both the trailing  $n_1$  upward branch and the leading low-level  $n_2$  branch (between the times of Figs. 20f,h). Extrema of  $\Delta z$  reach about  $+(-)$  270 m at 2.5 (7.5) km AGL. The altered soundings (Figs. 3, 11) show the features described by Mapes: a deepened boundary layer, low-level destabilization, and stabilization aloft. Profiles of CAPE and CIN (Fig. 24) confirm that the favorable effects in lower levels outweigh unfavorable effects aloft: CAPE is increased above the well-mixed layer and CIN decreases. ICAPE increases to 112% of its original value, and ICIN decreases to 52%. The change from the earlier suppressed state is even greater.

In the tropical atmosphere considered by Mapes (1993), with its lower level of free convection and less CIN, forcing of this magnitude might directly trigger further convection. In midlatitudes too, however, the forcing would certainly precondition the atmosphere for further convection (e.g., Crook and Moncrieff 1988), even if additional lifting by other mechanisms (e.g., cold pool outflows) was generally required for its activation.

This transient effect occurs earliest close to the central region and propagates outward with the  $n_2$  phase speed but with slightly less magnitude than illustrated above. This is because a low-level parcel, say at 40 km in Fig. 20f, has achieved maximum ascent due to the leading  $n_2$  branch, but the column has not yet benefited from the entire ascending  $n_1$  branch (cf. with Fig. 20d). Thus, after an ensemble undergoes a strong meso- $\beta$ -scale convective burst with both  $n_1$ - and  $n_2$ -like thermal forcing, destabilized low-level air with increased ICAPE is made available to the ensemble for convective reintensification. This response maximizes at about  $t = 1.5$  h at  $x = 20$  km for air drawn into the 0–20-km convective region and at about 2.0 h for the 20–50-km surrounding environment (Fig. 22f) or about 0.5 and 1.0 h, respectively, after the meso- $\beta$  convective maximum. This provides a positive feedback mechanism for convective reintensification that is consistent with the generalized timescale of the observed meso- $\beta$  cycle and regrowth in Fig. 1. This transient effect is qualitatively similar to the abruptly halted heating scenario of Mapes (1993, his Fig. 6), where the mechanism is illustrated at a later time and farther distance from the source (i.e., after the  $n_1$  gravity wave roll outruns the  $n_2$  roll, as in Figs. 20g,h).

As in Mapes (1993), this response to idealized heating was confirmed with simulations using a fully compressible, nonhydrostatic numerical model. Two- and three-dimensional (3D) versions of the Regional Atmospheric Modelling System (RAMS, described in NPC91) were used, initialized horizontally homogeneous with a convectively unstable troposphere and a deep stratospheric layer. A single thunderstorm, triggered by a warm bubble, was simulated. The response in the near environment showed outward-propagating zones of low- to midlevel convergence and upward displacements. Maximum  $\Delta z$  at a range of 75 km was approximately 200–300 m in 2D and 50–75 m in 3D. Additional thermal forcing by an ensemble of nearly in-phase cells could easily induce lifting several times these values.

Consider now the third heating scenario, the meso- $\beta$  cycle followed by regrowth, where the regrowth phase in the original source region is a plausible consequence of a positive feedback forced by the meso- $\beta$  burst itself. Instead of a descending low-level  $n_2$  branch restoring the parcels to their near-original level (e.g., at  $\sim 100$  km in Fig. 20h), an additional wave of low-level lifting is induced by the regrowth heating phase (see combined  $n_2$  curve in Fig. 19d and low-level ascent centers in Fig. 20j near  $x = 190$  and 120 km). Since the regrowth heating reaches a steady maximum, this effect is similar to the constant heating scenario of Mapes (1993, his Fig. 3). Like the first wave of low-level ascent, this second wave also propagates at the  $n_2$  phase speed and produces a quasi-steady level of maximum forced  $\Delta z$  (up to 360 m). This occurs by 3 h at  $x = 40$  km and spreads to  $x = 100$  km by 4 h. Thus, if the weakened ensemble does reintensify after the meso- $\beta$  convective

maximum, the near environment becomes favorably conditioned for the areal growth of convection, consistent with the generalized upscale growth sequence of MCCs described by MC92.

Recall that the system-wide meso- $\beta$  convective maxima in the MCSs were due to the more or less in-phase modulation in intensity in separated convective clusters. To examine the response to such a less concentrated meso- $\beta$  convective pulse, spatially and temporally staggered dual heat sources were examined. Each source had the same spatial width and duration dependencies as for the meso- $\beta$  burst with  $n1 + n2$  forcing in Fig. 19 except that  $Q_{m0}$  was halved, so that net heating from both sources was identical to the single burst. Linearized solutions were obtained for a variety of spatial separation of the sources' centers (up to 120 km) and temporal separation of their maximum forcing (up to 1 h). It was found that patterns of average divergence and  $w$  evolution, averaged over large regions containing both sources and over the intervening region between the sources, were similar to those for the meso- $\beta$  burst in Fig. 22. With increased spatial and temporal separation, the effects become weaker (by about half at maximum separations), are slower to develop (up to 1 h), and persist longer (up to 1 h). Thus, separated convective clusters acting somewhat in phase, as observed in the MCSs here and by MC92, could still induce a response that is favorable for convective reintensification and upscale growth.

## 6. Discussion

A conceptual model of a developing MCS is proposed in Fig. 25. It is intended to help explain, first, why the meso- $\beta$  convective cycle is a characteristic feature of upscale growth as in Fig. 1, as opposed to generally uninterrupted growth throughout the growth stage. Second, it illustrates the lagged response in the near environment which acts as a positive feedback mechanism for reintensification and upscale growth of the system.

A typical midlatitude MCS is considered. Four stages of development are illustrated at 30-min intervals, relative to the diabatic forcing (inset, Fig. 25a). West-east cross sections are shown through representative components of the convective ensemble and its developing stratiform region (see plan views). Weak to moderate environmental shear and some large-scale forcing (e.g., low-level convergence) are assumed. The wind profile (inset, Fig. 25b) is adapted from Houze et al. (1990) and is typical of that found in other studies of MCSs in the central United States (e.g., Maddox 1981; Bluestein and Jain 1985). Winds veer with height in the subcloud layer, with more unidirectional shear in the cloud layer. The depicted reference frame is moving eastward with the mean cell motion, about 5–10 m s<sup>-1</sup>. For simplicity, a heat source as in Fig. 19, centered at  $x = 0$ , is assumed to adequately represent the cumulative diabatic forcing of the near environment by the com-

ponent convective clusters. Also, gravity wave propagation is depicted for a troposphere with no shear and with constant stability. Schmidt and Cotton (1990) described the effects of shear on gravity wave propagation and how it affected their simulated squall line; those modifications, briefly discussed later, are not considered critical to the conceptual model here. The depicted flow in the plane is in fact highly 3D, including a component of low-level inflow from the south, flow around the convective cells, and radially propagating flow perturbations.

The first time is at  $t = 1.0$  h (Fig. 25a), when the rapidly developing convective ensemble has intensified to its maximum intensity in terms of net latent heating rate (maximum volumetric rain rate occurs with a slight lag). The ensemble consists of two or more convective clusters which persist for meso- $\beta$  timescales through the development stage. Cluster B is over a stable boundary layer (e.g., on the cold side of a front or over an old MCS cold pool) and is feeding off high- $\theta_e$  air flowing over the stable layer. Cluster D developed outside the cold air over an unstable boundary layer. McAnelly and Cotton (1986) and MC92 found that convection was often well organized into such multiple meso- $\beta$  entities in the developing MCCs they examined. While the distribution of these entities varies considerably from case to case depending on the mesoscale forcing (e.g., convergence along fronts, old outflow boundaries, and orographic upslope), this characterization is considered more general to MCS formation than the strictly linear distribution of isolated radar echoes ascribed by Leary and Houze (1979a) to the formative stages of squall lines. This characterization also implies larger and more persistent convective entities than the cells depicted in Bluestein and Jain's (1985) schematic modes of squall-line formation.

The two meso- $\beta$  clusters in Fig. 25a are depicted as nearly identical in structure and with in-phase maximum intensities. Widely variable structure is often observed (e.g., MC 92; Smull and Augustine 1993), and the phasing need only be sufficient (<1 h) so that rapid ensemble-wide intensification occurs. With the delayed development of strong precipitation and evaporational cooling, the  $n1$ -like heat source of the intensifying ensemble induces deep compensating subsidence, which first occurs individually around each strong cell or convective cluster (Fritsch 1975). As the convection intensifies toward  $t = 1$  h, the subsidence zones around the component clusters expand, unify, and collectively spread into the mesoscale environment as the leading subsidence branch of an  $n1$  gravity wave (Bretherton and Smolarkiewicz 1989; NPC91). Relative to this locally warmed environment, parcels in the convective updrafts are less buoyant, and the ensemble begins weakening. Thus, the subsidence induced by the intensifying ensemble first acts as a negative feedback that weakens the convection (Fig. 25b), resulting in the characteristic decreasing volumetric rain rate after a meso-

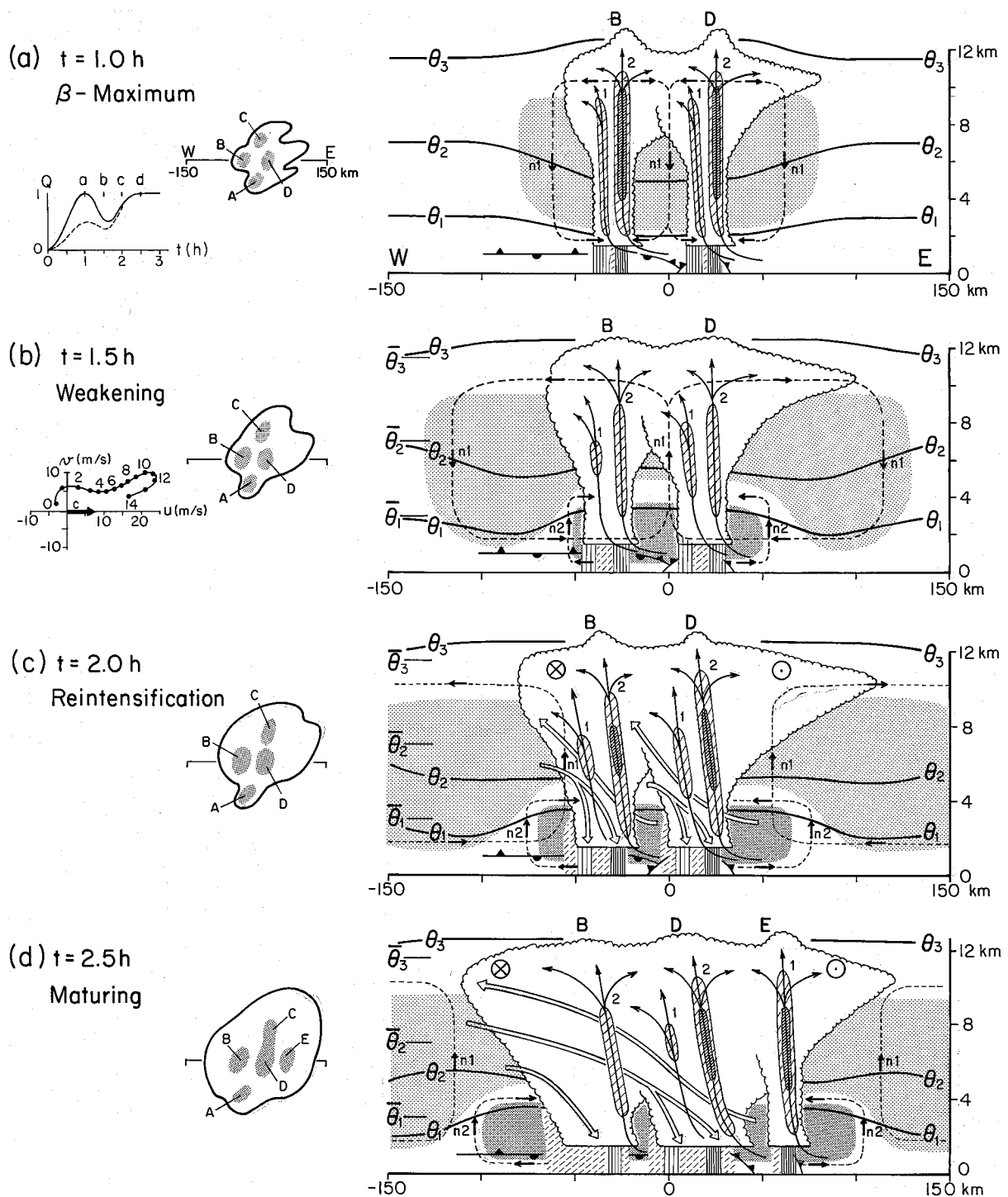


FIG. 25. Conceptual model of MCS development and its relation to the meso- $\beta$  convective cycle. Panels (a)–(d) are at times 1.0, 1.5, 2.0, and 2.5 h, respectively, relative to time-dependent  $n_1 + n_2$  forcing from Fig. 19d [see inset in (a)]. Small plan views show the spatial distribution of meso- $\beta$  convective components (labeled A–E) that form the convective ensemble; outer contour is outline of the cirrus cloud shield. The reference frame is moving eastward with cell velocity  $C$  [see environmental hodograph inset in (b)]; heights are in kilometers AGL. West–east cross sections depict flow in the  $x$ – $z$  plane through meso- $\beta$  components B and D [and E in (d)]; each component consists of individual cells numbered by order of origin. Thin solid streamlines are storm-relative and depict primary updrafts through cells; light and dark hatching denotes  $w > 10$  and  $20 \text{ m s}^{-1}$ , respectively. In (c) and (d), open arrows depict storm-relative mesoscale flow and transverse anticyclonic flow is indicated aloft. Dashed streamlines depict linearized gravity wave flow perturbations (due to meso- $\beta$  burst only) emanating from the thermally forced region; short arrows show positions of maximum flow perturbations. In (a),  $n_1$  subsidence is depicted for each cluster; in (b)–(d), ensemble-scale  $n_1$  circulation and leading, low-level  $n_2$  ascent are depicted. Low-, middle- and upper-tropospheric potential

$\beta$  maximum. During this decrease, condensate from rearward drifting decayed cells (e.g., Leary and Houze 1979a) and from ongoing but weakened convection results in a continuing areal increase of the cloud shield, echo aloft, and oftentimes surface precipitation.

Other factors could also cause this weakening: an exhaustion of low-level high- $\theta_e$  air; reduced buoyancy of this inflow air due to evaporation and water loading; dynamic entrainment of lower  $\theta_e$  air due to nonhydrostatic pressure perturbations and shear; and cold pool outflows cutting off inflow to the convective cells (Cotton and Anthes 1989). However, convective-scale propagation into the low-level flow, which is facilitated by vertical wind shear, can offset these latter mechanisms (e.g., Thorpe et al. 1982; Weisman et al. 1988; Rotunno et al. 1988). Furthermore, there is no reason for these mechanisms, operating independently in the component clusters, to be generally in-phase in a manner that would coherently weaken the entire ensemble. These mechanisms are considered here to act as finer-scale controls on the intensity of individual cells and to affect the structure of the individually evolving clusters. Conversely, the subsidence warming by the ensemble could weaken all components of the ensemble simultaneously. In fact, this subsidence could be a self-phasing mechanism. Subsidence from an initially stronger cluster would lead to a weakening of itself and any others nearby; the slightly lagged intensification of a second comparable cluster would be suppressed by subsidence from the first, causing the second cluster's maximum to occur earlier and more in-phase with the first cluster.

The forced subsidence expands until some time after the meso- $\beta$  maximum, creating a large meso- $\beta$ -scale region that is positively buoyant relative to the larger-scale environment. The reduced diabatic forcing cannot maintain the buoyancy perturbation, and mesoscale ascent ensues with the excitation of a meso- $\beta$   $n1$  gravity wave. This is the "intermediate scale circulation" that Fritsch (1975) hypothesized would favor reintensification of the convective ensemble. The linearized analysis in section 5 suggests that by itself, the ascending branch of the  $n1$  wave would only lift the subsidence region back to its original level and would not favor further convection. However, in concert with any continuing larger-scale forcing that helped trigger the initial ensemble and with other processes discussed below, this meso- $\beta$ -scale ascent would favor reintensification of the ensemble. Such larger-scale forcing for an orogenic MCS simulated by Tripoli and Cotton (1989a,b) was provided by a persistent mountain-plains convergence zone. They related the system's  $\sim 2$ -h self-modulating periodicity in intensity to meso- $\beta$ -scale subsidence warming around the ensemble and the periodic "re-

bound" in the core region as deep tropospheric gravity waves were shed.

Many studies indicate that higher-order gravity waves associated with evaporational cooling also play a critical role in MCS development and structure (e.g., Raymond 1987; Tripoli and Cotton 1989b; Schmidt and Cotton 1990; Mapes 1993). Concurrent with the spreading subsidence aloft in Figs. 25a and b, the strong precipitation produced by the intensification phase leads to increased low-level evaporational cooling. An  $n2$  (or higher order; Mapes 1993) gravity wave is initiated by the evaporational cooling and, like the  $n1$  wave, modifies a meso- $\beta$ -scale region that affects the entire ensemble. The  $n2$ -induced low-level ascent trails the  $n1$  descent due to its lagged development and its slower phase speed. [In Schmidt and Cotton's (1990) squall-line simulations, increased shear resulted in a Doppler shifting of the leading low-level  $n2$  gravity wave and kept its ascending branch closer to the leading convection.] This "compensating ascent" by the  $n2$  mode is of greater magnitude than the  $n1$  descent in low levels, resulting in the negatively buoyant region depicted at  $t = 1.5$  h in Fig. 25b. Through the forced lifting, the depth of the low-level layer of high- $\theta_e$  air, CAPE and ICAPE all increase, and CIN and ICIN decrease (Mapes 1993). The low-level destabilization of the near environment is thus a positive feedback that favors reintensification of the ensemble, depicted at  $t = 2$  h in Fig. 25c.

The role of evaporationally induced surface outflows on the maintenance and structure of MCSs (primarily squall lines) has been stressed in many nonhydrostatic modeling studies (e.g., Thorpe et al. 1982; Weisman et al. 1988; Rotunno et al. 1988; Fovell and Ogura 1989; Lafore and Moncrieff 1989; Weisman 1992, 1993). These studies show that outflows, which can be strengthened by rear inflow into the stratiform region in mature systems, interact with certain sheared environments to provide optimum forced lifting for intense, long-lived systems. However, there is evidence that gust front-shear interaction may be insufficient to account for MCS development in general. Crook and Moncrieff (1988) found that long-lived convection could be maintained in simulations with no evaporation and thus no outflow forcing, provided that large-scale forcing was present, which is often the case. Many MCSs form and remain poleward of a surface front over cool air in which strong density currents would not form (e.g., Johns and Hirt 1987; Schmidt and Cotton 1989; Stumpf et al. 1991; Fortune et al. 1992; Trier and Parson 1993; Nachamkin et al. 1994). Finally, some MCSs exhibit a form of discrete propagation on the meso- $\beta$  scale: system motion is faster than any sustained outflow forcing and is due to the successive development of meso- $\beta$  convective

---

isotherms are labeled  $\theta_1$ ,  $\theta_2$ , and  $\theta_3$ , respectively; their ambient levels in (b)–(d) are denoted by overbars. Light (medium) shading denotes positive (negative) buoyancy perturbations induced by  $n1$  subsidence (low-level  $n2$  ascent). Convective rain intensity (vertical hatching) is proportional to updraft  $w$  and  $n1$  heating. Stratiform rain is depicted by diagonal hatching.

entities well ahead of existing convective outflows (McAnelly and Cotton 1986; Fortune et al. 1992; Cram et al. 1992a; Stensrud and Fritsch 1993).

Without discounting the controlling influence of outflow dynamics on the overall evolution of certain classes of squall lines (particularly during their mature stage), gust front forcing during the early reintensification stage here is considered to act more on the local scale of individual cells and clusters than on the "global" scale of the system (e.g., Lafore and Moncrieff 1989). Gust front forcing may be the necessary means by which individual clusters propagate and persist rather than dissipate, but it is the ensemble-scale response to the meso- $\beta$  burst thermal forcing that primes the entire region for vigorous growth. In Fig. 25c, the leading gust front is a local forcing mechanism that helps reintensify cluster D by efficiently lifting the preconditioned inflow into cell D2. Cluster B is reintensifying to a lesser extent due to the increased ICAPE but without strong gust front forcing.

Although the low-level outflow perturbation induced by the  $n2$  mode reduces the relative inflow strength (by about  $1\text{--}2\text{ m s}^{-1}$ ) ahead of the system in Fig. 25c, this inflow has more ICAPE, and relative inflow could increase through faster propagation. Raymond (1984, 1987), in his forced gravity wave model of convection, found that after the strong advective instability mode weakened, propagation speeds increased when the system reintensified into a long-lived propagating mode. These modes apparently are manifestations of the observed meso- $\beta$  convective burst and regrowth into a mature system, respectively. Cram et al. (1992a,b) found evidence of this propagating mode in their analysis and simulation of a squall line case. The faster mode is consistent with the discrete meso- $\beta$ -scale propagation observed by McAnelly and Cotton (1986) and Fortune et al. (1992). The faster propagation is also consistent with the analysis by Rasmussen and Rutledge (1993), who observed that squall-line propagation speeds increased rapidly after the transition from intensifying to mature stages (possibly due to strengthened gust front forcing). The end of their intensifying stage was marked by maximum line-averaged updraft intensity, which might correspond to the meso- $\beta$  convective maximum. The transition to their mature stage marked the beginning of a rearward tilt of previously upright updraft structure, with ascending front-to-rear flow and descending rear-to-front flow becoming organized. The reintensified convective updrafts in Fig. 25c display this increased tilt and developing mesoscale flow branches are depicted.

Another important effect of the  $n2$  mode is to raise the strong convergence initially at low levels into midlevels (cf. Figs. 25a with 25b,c). Since MCSs tend to form in environments with deep moisture (Cotton and Anthes 1989), the increased inflow at midlevels has less detrimental drying effects on the system than would occur with less midlevel moisture. With the increased

midlevel inflow, various ascending and descending flow branches become better organized. These can vary greatly, depending on thermodynamic and shear profiles. Analysis of simulated and observed MCSs has shown that midlevel inflow from both front and rear (and laterally) can be transported both up and down within the system (Weisman et al. 1988; Lafore and Moncrieff 1989; Schmidt and Cotton 1989; Tripoli and Cotton 1989a; Verlinde and Cotton 1990; Nachamkin et al. 1994). In Fig. 25c, midlevel inflow is depicted as developing into the typical ascending front-to-rear and descending rear-to-front flow branches (e.g., Houze et al. 1989).

After reintensification of the convective ensemble, low-level lifting by the  $n2$  gravity waves (Fig. 20j) continues propagating into the environment. Air feeding the MCS has thus been favorably conditioned for convection, and ongoing growth toward a mature MCS continues. In Fig. 25d, a new meso- $\beta$  convective cluster (cell E1) has developed ahead of the leading gust front forcing. This typifies the areal growth of convection seen after the meso- $\beta$  convective cycle (MC92) and the discrete meso- $\beta$ -scale propagation discussed by McAnelly and Cotton (1986) and Fortune et al. (1992). During this growth, mesoscale flow branches become more extensive and better organized. Within the expanding stratiform echo, hydrometeor growth in the ascending front-to-rear flow contributes to the system-wide diabatic heating, and cooling due to evaporation and melting induces more organized mesoscale descent; midlevel convergence increases further (Leary and Houze 1979b; Rutledge and Houze 1987). Upper-level anticyclonic flow develops in association with strong divergence from an upper-tropospheric mesohigh. [As reviewed by Verlinde and Cotton (1990), the development of midlevel cyclonic flow in MCSs generally occurs in more mature to weakening stages.] Schmidt and Cotton's (1990) squall-line simulation in strong shear showed that the upstream propagating  $n1$  gravity wave effectively blocked the strong mid- to upper-level ambient flow from reaching the system. In conjunction with an upstream propagating low-level gravity wave, midlevel flow approaching the system was channelled into a well-organized rear inflow jet. Nachamkin et al. (1994) observed such upper-level blocking and the development of descending rear inflow in a developing MCS.

This conceptual model of MCS development hypothesizes that rapid intensification of a meso- $\beta$  convective ensemble induces a thermally forced, self-modulating mechanism that helps explain the characteristic upscale evolution observed in some MCSs. Many multicell clusters and small, short-lived MCSs may go through the initial meso- $\beta$  burst without reintensifying or evolving upscale to much degree. The two small MCSs described here showed only modest reintensification. Some longer-lived MCSs may evolve through successive meso- $\beta$  cycles, or may consist of component clusters that evolve through their individual cycles, where upscale

evolution occurs in steps in association with each. Still other MCSs may exhibit more gradual, monotonic growth to mature stage without any meso- $\beta$  pulsing. Most previous conceptual models of MCS growth, either explicitly or implicitly, invoke the latter scenario (e.g., Maddox 1980; Zipser 1982; Houze et al. 1989).

To the extent that an early meso- $\beta$ -scale convective cycle is a generalized feature in MCS growth, its dynamic role in overall system evolution probably ranges from inconsequential to significant. For a strongly forced, intense MCS, the meso- $\beta$  cycle could reflect simply a temporary modulation of its growth. Its initial explosive growth cannot continue unabated due to the intense subsidence warming. The warm anomaly must be transmitted away by a deep  $n1$  gravity wave before the system's growth can continue, and with the favorably modified environment by the  $n2$  mode, this growth can endure relatively uninterrupted. In more weakly forced situations where convection is more widespread or develops less explosively, a meso- $\beta$  cycle might provide a critical self-organizing mechanism for MCS growth. Consider a field of ordinary convective clusters, developing and evolving independently. Then two or more clusters happen to intensify in close spatial and temporal proximity. The response in the near environment to their collective diabatic forcing could be critical to their unified reintensification into a mature MCS, at the expense of more distant clusters.

*Acknowledgments.* This work was supported by the National Science Foundation, under Grants ATM-9118963 and ATM-9420045, and through a 20-h mini-grant from the CSU-CHILL Cooperative Agreement ATM-8919080. Thanks are extended to Steve Rutledge, Pat Kennedy, Dave Brunkow, and Ken Pattison (CSU-CHILL) for field project support; Bob Rilling and Peter Neilley (NCAR) for MHR and mesonet data, respectively; Nan McClurg and Steve Finley (CSU), respectively, for satellite and NWS data and analysis software; Doug Burks (CSU) and Michele Case (NCAR) for radar analysis software; and Judy Sorbie-Dunn (CSU) for drafting. Formal reviews by two anonymous reviewers, and informal reviews by Brian Mapes and Jerry Schmidt, are greatly appreciated and were very helpful in improving the paper.

#### REFERENCES

- Bluestein, H. B., and M. H. Jain, 1985: Formation of mesoscale lines of precipitation: Severe squall lines in Oklahoma during the spring. *J. Atmos. Sci.*, **42**, 1711–1732.
- Bretherton, C. S., and P. K. Smolarkiewicz, 1989: Gravity waves, compensating subsidence, and detrainment around cumulus clouds. *J. Atmos. Sci.*, **46**, 740–759.
- Cotton, W. R., and R. A. Anthes, 1989: *Storm and Cloud Dynamics*. Academic Press, 883 pp.
- Cram, J. M., R. A. Pielke, and W. R. Cotton, 1992a: Numerical simulation and analysis of a prefrontal squall line. Part I: Observations and basic simulation results. *J. Atmos. Sci.*, **49**, 189–208.
- , —, and —, 1992b: Numerical simulation and analysis of a prefrontal squall line. Part I: Propagation of the squall line as an internal gravity wave. *J. Atmos. Sci.*, **49**, 209–225.
- Crook, N. A., and M. W. Moncrieff, 1988: The effect of large-scale convergence on the generation and maintenance of deep moist convection. *J. Atmos. Sci.*, **45**, 3606–3624.
- Fortune, M. A., W. R. Cotton, and R. L. McAnelly, 1992: Frontal wave-like evolution in some mesoscale convective complexes. *Mon. Wea. Rev.*, **120**, 1279–1300.
- Fovell, R. G., and Y. Ogura, 1989: Effect of vertical wind shear on numerically simulated multicell storm structure. *J. Atmos. Sci.*, **46**, 3144–3176.
- Fritsch, J. M., 1975: Cumulus dynamics: Local compensating subsidence and its implications for cumulus parameterization. *Pure Appl. Geophys.*, **113**, 851–867.
- Houze, R. A., Jr., S. A. Rutledge, M. I. Biggerstaff, and B. F. Smull, 1989: Interpretation of Doppler weather radar displays of mid-latitude mesoscale convective systems. *Bull. Amer. Meteor. Soc.*, **70**, 608–619.
- , B. F. Smull, and P. Dodge, 1990: Mesoscale organization of springtime rainstorms in Oklahoma. *Mon. Wea. Rev.*, **118**, 613–654.
- Johns, R. H., and W. D. Hirt, 1987: Derechos: Widespread convectively induced windstorms. *Wea. Forecasting*, **2**, 32–49.
- Kennedy, P. C., and S. A. Rutledge, 1995: Dual-Doppler and multiparameter radar observations of a bow-echo hailstorm. *Mon. Wea. Rev.*, **123**, 921–943.
- Lafore, J.-P., and M. W. Moncrieff, 1989: A numerical investigation of the organization and interaction of the convective and stratiform regions of tropical squall lines. *J. Atmos. Sci.*, **46**, 521–544.
- Leary, C. A., and R. A. Houze Jr., 1979a: The structure and evolution of convection in a tropical cloud cluster. *J. Atmos. Sci.*, **36**, 437–457.
- , and —, 1979b: Melting and evaporation of hydrometeors in precipitation from the anvil clouds of deep tropical convection. *J. Atmos. Sci.*, **36**, 669–679.
- Maddox, R. A., 1980: Mesoscale convective complexes. *Bull. Amer. Meteor. Soc.*, **61**, 1374–1387.
- , 1981: The structure and life-cycle of midlatitude mesoscale convective complexes. Dept. Atmospheric Sciences Paper 336, 331 pp. [Available from Department Atmospheric Sciences, Colorado State University, Fort Collins, CO 80523.]
- Mapes, B. E., 1993: Gregarious tropical convection. *J. Atmos. Sci.*, **50**, 2026–2037.
- McAnelly, R. L., and W. R. Cotton, 1986: Meso- $\beta$ -scale characteristics of an episode of meso- $\alpha$ -scale convective complexes. *Mon. Wea. Rev.*, **114**, 1740–1770.
- , and —, 1992: Early growth of mesoscale convective complexes: A meso- $\beta$ -scale cycle of convective precipitation? *Mon. Wea. Rev.*, **120**, 1851–1877.
- Miller, L. J., C. G. Mohr, and A. J. Weinheimer, 1986: The simple rectification to Cartesian space of folded radial velocities from Doppler radar sampling. *J. Atmos. Oceanic Technol.*, **3**, 162–174.
- Mohr, C. G., L. J. Miller, R. L. Vaughan, and H. W. Frank, 1986: The merger of mesoscale datasets into a common Cartesian format for efficient and systematic analyses. *J. Atmos. Oceanic Technol.*, **3**, 143–161.
- Nachamkin, J. E., R. L. McAnelly, and W. R. Cotton, 1994: An observational analysis of a developing mesoscale convective complex. *Mon. Wea. Rev.*, **122**, 1168–1188.
- Nicholls, M. E., R. A. Pielke, and W. R. Cotton, 1991: Thermally forced gravity waves in an atmosphere at rest. *J. Atmos. Sci.*, **48**, 1869–1884.
- Oye, D., and M. Case, 1992: REORDER—A program for gridding radar data: Installation and use manual for the UNIX version, 22 pp. [Available from National Center for Atmospheric Research, Field Observing Facility, P.O. Box 3000, Boulder, CO 80307.]

- Oye, R., and R. Carbone, 1981: Interactive Doppler editing software. Preprints, *20th Conf. on Radar Meteorology*, Boston, MA, Amer. Meteor. Soc., 683–689.
- Pandya, R., D. Duran, and C. Bretherton, 1993: Comments on “Thermally forced gravity waves in an atmosphere at rest.” *J. Atmos. Sci.*, **50**, 4097–4101.
- Pratte, J. F., J. H. Van Andel, D. G. Ferraro, R. W. Gagnon, S. M. Maher, and G. L. Blair, 1991: NCAR’s mile high meteorological radar. Preprints, *25th Conf. on Radar Meteorology*, Paris, France, Amer. Meteor. Soc., 863–866.
- Rasmussen, E. N., and S. A. Rutledge, 1993: Evolution of quasi-two-dimensional squall lines. Part I: Kinematic and reflectivity structure. *J. Atmos. Sci.*, **50**, 2584–2606.
- Raymond, D. J., 1983: Wave-CISK in mass-flux form. *J. Atmos. Sci.*, **40**, 2561–2572.
- , 1984: A wave-CISK model of squall lines. *J. Atmos. Sci.*, **41**, 1946–1958.
- , 1986: Prescribed heating of a stratified atmosphere as a model for moist convection. *J. Atmos. Sci.*, **43**, 1101–1111.
- , 1987: A forced gravity wave model of self-organizing convection. *J. Atmos. Sci.*, **44**, 3528–3543.
- Rotunno, R., J. B. Klemp, and M. L. Weisman, 1988: A theory for strong, long-lived squall lines. *J. Atmos. Sci.*, **45**, 463–485.
- Rutledge, S. A., and R. A. Houze Jr., 1987: A diagnostic modelling study of the trailing stratiform region of a midlatitude squall line. *J. Atmos. Sci.*, **44**, 2640–2656.
- , P. C. Kennedy, and D. A. Brunkow, 1993: Use of the CSU-CHILL radar in radar meteorology education at Colorado State University. *Bull. Amer. Meteor. Soc.*, **74**, 25–31.
- Schmidt, J. M., and W. R. Cotton, 1989: A High Plains squall line associated with severe surface winds. *J. Atmos. Sci.*, **46**, 281–302.
- , and —, 1990: Interactions between upper and lower tropospheric gravity waves on squall line structure and maintenance. *J. Atmos. Sci.*, **47**, 1205–1222.
- Scott, J. D., and S. A. Rutledge, 1995: Doppler radar observations of an asymmetric mesoscale convective system and associated vortex couplet. *Mon. Wea. Rev.*, **123**, 3437–3457.
- Smull, B. F., and J. A. Augustine, 1993: Multiscale analysis of a mature mesoscale convective system. *Mon. Wea. Rev.*, **121**, 103–132.
- Stensrud, D. K., and J. M. Fritsch, 1993: Mesoscale convective systems on weakly forced large-scale environments. Part I: Observations. *Mon. Wea. Rev.*, **121**, 3326–3344.
- Stumpf, G. J., R. H. Johnson, and B. F. Smull, 1991: The wake low in a midlatitude mesoscale convective system having complex convective organization. *Mon. Wea. Rev.*, **119**, 134–158.
- Thorpe, A. J., M. J. Miller, and M. W. Moncrieff, 1982: Two-dimensional convection in non-constant shear: A model of midlatitude squall lines. *Quart. J. Roy. Meteor. Soc.*, **108**, 739–762.
- Trier, S. B., and D. B. Parsons, 1993: Evolution of environmental conditions preceding the development of a nocturnal mesoscale convective complex. *Mon. Wea. Rev.*, **121**, 1078–1098.
- Tripoli, G., and W. R. Cotton, 1989a: Numerical study of an observed orogenic mesoscale convective system. Part 1: Simulated genesis and comparison with observations. *Mon. Wea. Rev.*, **117**, 273–304.
- , and —, 1989b: Numerical study of an observed orogenic mesoscale convective system. Part 2: Analysis of governing dynamics. *Mon. Wea. Rev.*, **117**, 305–328.
- Verlinde, J., and W. R. Cotton, 1990: A mesoscale vortex couplet observed in the trailing anvil of a multicellular convective complex. *Mon. Wea. Rev.*, **118**, 993–1010.
- Weisman, M. L., 1992: The role of convectively generated rear-inflow jets in the evolution of long-lived mesoconvective systems. *J. Atmos. Sci.*, **49**, 1826–1847.
- , 1993: The genesis of severe, long-lived bow echoes. *J. Atmos. Sci.*, **50**, 645–670.
- , J. B. Klemp, and R. Rotunno, 1988: Structure and evolution of numerically simulated squall lines. *J. Atmos. Sci.*, **45**, 1990–2013.
- Zipser, E. J., 1982: Use of a conceptual model of the life-cycle of mesoscale convective systems to improve very-short-range forecasts. *Nowcasting*, K. A. Browning, Ed., Academic Press, 191–204.